[redacted]

OAK RIDGE NATIONAL LABORATORY
operated by
UNION CARBIDE CORPORATION
for the
U. S. ATOMIC ENERGY COMMISSION

ORNL-TM-2803

PERFORMANCE CHARACTERISTICS OF CYLINDRICAL HEAT PIPES FOR NUCLEAR ELECTRIC SPACE AND UNDERSEA POWER PLANTS

M. E. LaVerne

NOTICE This document contains information of a preliminary nature and was prepared primarily for internal use at the Oak Ridge National Laboratory. It is subject to revision or correction and therefore does not represent a final report.

This report was prepared as an account of work sponsored by the United States Government. Neither the United States nor the United States Atomic Energy Commission, nor any of their employees, nor any of their contractors, subcontractors, or their employees, makes any warranty, express or implied, or assumes any legal liability or responsibility for the accuracy, completeness or usefulness of any information, apparatus, product or process disclosed, or represents that its use would not infringe privately owned rights.

ORNL TM-2803

Contract No. W-7403-eng-26

REACTOR DIVISION

PERFORMANCE CHARACTERISTICS OF CYLINDRICAL HEAT PIPES FOR NUCLEAR ELECTRIC SPACE AND UNDERSEA POWER PLANTS

M. E. LaVerne

JANUARY 1971

OAK RIDGE NATIONAL LABORATORY
Oak Ridge, Tennessee
operated by
UNION CARBIDE CORPORATION
for the
U. S. ATOMIC ENERGY COMMISSION

CONTENTS

	Page
ABSTRACT	1
INTRODUCTION	1
HEAT PIPE OPERATING PRINCIPLES	3
FLUID PROPERTIES	5
Surface Tension	5
Latent Heat	5
Density	5
Viscosity	12
Vapor Pressure	12
CAPILLARY STRUCTURES	12
Screen Wicks	14
Longitudinal Channels	15
Artery	16
Annulus	18
Other Structures	19
OPERATING EXPERIENCE	19
HEAT TRANSPORT LIMITATIONS	22
Sonic Flow	23
Startup	29
Entrainment	31
Capillary Pumping	35
Capillary Pressure Rise	35
Liquid Pressure Drop	35
Vapor Pressure Drop	36
Overall Pressure Balance	38
Comparison with Experiment	39
Flow Stability	41
OPTIMIZATION OF CAPILLARY LIMITED HEAT PIPES	42
Mesh and Channel Wicks	42
Optimum Capillary Radius	42
Optimum Radius Ratio	45
Screened Annulus	45

Page

EFFECTS OF HEAT PIPE PARAMETERS 48

Geometric Effects 48

Diameter 48

Length 50

Annulus Eccentricity 52

Attitude 52

Fluid Effects 54

SUMMARY 57

REFERENCES 61

Appendix A — FORTRAN SUBROUTINES FOR COMPUTING THE THERMODYNAMIC AND TRANSPORT PROPERTIES OF CESIUM, POTASSIUM, SODIUM, AND LITHIUM 67

Appendix B — NOMENCLATURE 71

LIST OF FIGURES

Figure		Page
1	Schematic Longitudinal Cross-Section of a Heat Pipe	4
2	Surface Tensions for Cesium, Potassium, Sodium, and ..... Lithium as Functions of Vapor Temperature	6
3	Latent Heats for Cesium, Potassium, Sodium, and Lithium ... as Functions of Vapor Temperature	7
4	Liquid Densities for Cesium, Potassium, Sodium, and ..... Lithium as Functions of Vapor Temperature	8
5	Vapor Densities for Cesium, Potassium, Sodium, and ..... Lithium as Functions of Vapor Temperature	9
6	Liquid and Vapor Viscosities for Cesium, Potassium, ... Sodium, and Lithium as Functions of Vapor Temperature	10
7	Vapor Pressure of Cesium, Potassium, Sodium, and ..... Lithium as Functions of Vapor Temperature	11
8	Some Examples of Heat Pipe Capillary Structures	13
9	Effect of Channel Screen Cover on Axial Heat Flow in a .... Sodium Heat Pipe	17
10	Comparison of Calculated and Experimental Sonic Limits .... on Axial Heat Flow for Cesium, Potassium, and Sodium Heat Pipes. Calculated values only for lithium.	25
11	Evaporator Pressure Ratio as a Function of Sonic Heat ..... Transport Fraction. Comparison of calculated values with experimental data for cesium and sodium.	26
12	Calculated Evaporator Temperature Drop at Sonic Flow as ... a Function of Maximum Evaporator Temperature for Cesium, Potassium, Sodium, and Lithium	28
13	Comparison of Calculated and Experimental Entrainment- .... Limited Output of a Sodium Heat Pipe. Characteristic dimension selected for best fit.	33
14	Entrainment Parameter Based on Weber Number, Propor- ..... tional to Heat Pipe Output at Entrainment Limit for Cesium, Potassium, Sodium, and Lithium	34
15	Comparison of Calculated and Experimental Output of ..... a Heat Pipe, Taking into Account the Sonic, Entrainment, and Capillary Limits	40

Figure		Page
16	Heat Pipe Output as a Function of Vapor Temperature and Capillary Width. Ratio of wall radius to vapor radius = 1.2. Fluid = Cesium.	43
17	Optimization of Annulus Width in a Screened Annulus Heat Pipe for Several Vapor Temperatures	47
18	Heat Pipe Output as a Function of Vapor Radius for Several Subsidiary Constraints	49
19	Heat Pipe Output as a Function of Effective Length for Several Annulus Widths	51
20	Calculated Effect on Heat Pipe Output of Orientation in a 1-g Field	53
21	Experimental Effect on Heat Pipe Output of Orientation in a 1-g Field	55
22	Working Fluid Performance Parameter Based on Use in an Optimized Heat Pipe	56

PERFORMANCE CHARACTERISTICS OF CYLINDRICAL HEAT PIPES FOR NUCLEAR ELECTRIC SPACE AND UNDERSEA POWER PLANTS

M. E. LaVerne

ABSTRACT

A preliminary investigation was made of the performance characteristics of cylindrical heat pipes with a view toward their incorporation as heat transport devices in nuclear electric space and undersea power plants, where reliable unattended operation is of prime importance.

The basic operating principles of the heat pipe were set forth, together with an enumeration of the pertinent thermodynamic and transport fluid properties and a brief discussion of each. A number of capillary structures, of both the simple and composite type, was described and some of the advantages and disadvantages were delineated. The readily available heat pipe operating lifetime data were reviewed and were summarized in tabular form. The data show that the heat pipe is capable of the long-term reliability required for unattended operation.

The theoretical bases for predicting several of the inherent heat pipe performance limits were reviewed and the resulting predictions compared with experimental data. In general, theory and experiment compare quite well.

The optimization of heat pipe geometry with respect to performance was shown for the situation where heat pipe output is not limited by compressibility or entrainment effects. Finally, the effects of several geometric and fluid parameters were examined, primarily by means of the theoretical relations previously obtained.

INTRODUCTION

The potential attractiveness of the "heat Pipe"[1] for heat transport in nuclear electric space and undersea power plants stems from a number of intrinsic properties of the device. First, the effective thermal conductance is extremely high because the heat is transported as the latent heat of the fluid. Second, because the evaporation and condensation take place essentially independently, coupling of a heat source and sink with

widely different characteristics is possible, i.e., the heat pipe serves as a heat flux transformer. Also, the source and sink may be separated some distance from each other without temperature degradation, thus allowing, for example, efficient removal of heat through a nuclear radiation shield. Finally, inasmuch as the heat pipe is completely self-contained and, therefore, not dependent on any external electrical or mechanical device for continued operation, its inherent reliability can be made quite high.

A preliminary investigation, therefore, has been made of the performance characteristics of the heat pipe with a view toward its use as a nuclear electric space and undersea power plant heat transport device. The analytical portion of the investigation is based primarily on the theory developed by Cotter[2] and extended by Kemme[3,4] at Los Alamos Scientific Laboratory (LASL). Because of their ready availability in the open literature and general clarity of presentation, LASL experimental results[3-5] were relied upon for comparison with computed results.

Although heat pipe size and shape are, at least in principle, quite arbitrary, attention has been confined here to a simple, long, circular cylinder. Similarly, of the multitude of possible capillary structures, only longitudinal rectangular grooves and a screened annulus have been analyzed in this report.

Because of the inherently high operating temperatures associated with power generation in, for example, thermoelectric or thermionic devices, the alkali metals are prime candidates for heat pipe working fluids. Thermodynamic and heat transfer properties have been obtained for cesium, potassium, sodium, and lithium from a number of sources.[6-17] These properties have been incorporated into FORTRAN subroutines for use with computer design programs. These subroutines are listed in Appendix A.

The results can be used to define the heat transport limitations for a series of heat pipe geometry and fluid combinations and operating conditions. In effect, this provides a basis for the preparation of a series of reference designs.

HEAT PIPE OPERATING PRINCIPLES

Figure 1 shows a schematic longitudinal cross section of a heat pipe. The heat pipe consists essentially of a sealed container lined with a relatively thin suitable capillary structure. The capillary structure, or wick, is saturated with a wetting liquid and the remaining volume contains the vapor phase of the working fluid. The insulated section indicated in the figure is provided to allow for the length required for shield penetration if the heat pipe is used with a nuclear reactor or isotope heat source.

In steady operation, the temperature in the evaporator is maintained slightly higher than in the condenser by means of a heat source. This temperature difference results in a vapor pressure difference which drives the vapor from evaporator to condenser. As a result of the depletion of liquid by evaporation, the vapor-liquid interface in the evaporator retreats into the capillary structure, where the typical meniscus assumes a radius of curvature on the order of the largest capillary pore radius. Similarly, accumulation of the liquid in the condenser section will cause the meniscus there to assume some relatively large radius, typically on the order of the radius of the pipe. The resulting difference in radii of curvature at the two liquid-vapor interfaces then produces a surface tension force which drives the liquid through the capillary structure from the condenser to the evaporator against the viscous retarding force and possible gravitational forces, thus completing the flow cycle. For steady operation, the integrated pressure drop around the entire flow circuit must obviously be zero.

As the heat load is increased, the menisci in the evaporator section will retreat farther into the capillary structure until they attain some minimum value characteristic of the wick. At this point, the available capillary driving force has attained its maximum and the pipe is transferring heat at its maximum possible rate. Thus, the heat pipe is capable, at a particular operating temperature, of transferring heat at any rate between zero and some maximum value characterized by the detailed capillary structure.

ORNL DWG 70-15209

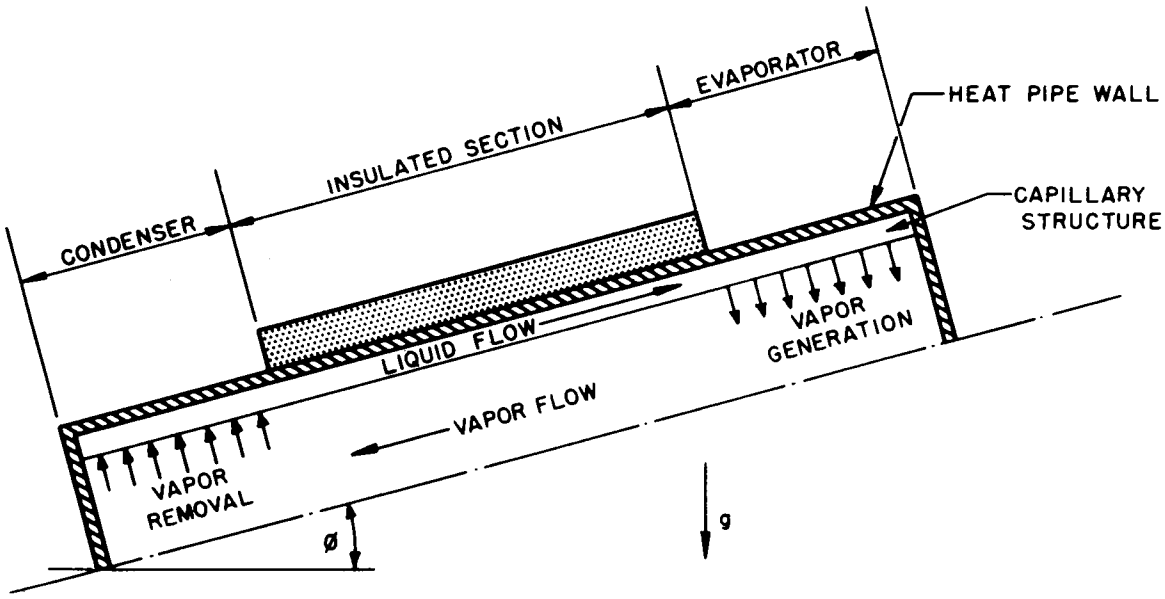

Fig. 1. Schematic Longitudinal Cross-Section of a Heat Pipe.

FLUID PROPERTIES

Fluid thermodynamic and transport properties pertinent to heat pipe operation are presented in Figs. 2 through 7 for cesium, potassium, sodium, and lithium as functions of vapor temperature. Because of the operating principle of the heat pipe, desirable properties for working fluids are: (1) high surface tension; (2) high latent heat of vaporization; (3) high density, at least in the vapor phase; (4) low viscosity; (5) moderate vapor pressure.

Surface Tension

Surface tension provides the essential driving force for liquid flow in the wick. Obviously, high surface tension then means high liquid recirculation rates. This, however, is not the entire story. Wetting ability, as measured by the contact angle between the liquid vapor interface and the contacting surface, is also a factor. In fact, one might define an "effective surface tension" as the product of the surface tension and the cosine of this angle of contact.

Latent Heat

A high latent heat of vaporization is desirable in order to minimize the mass flow of fluid required in order to transport a given amount of heat.

Density

Both frictional and momentum pressure drops in the vapor phase are inversely proportional to vapor density. Vapor pressure drop is therefore minimized by a high vapor density.

Similarly, a high liquid density minimizes frictional pressure drop in the capillary structure and is, therefore, desirable on that account. However, where operation of a very long heat pipe in a gravity field is

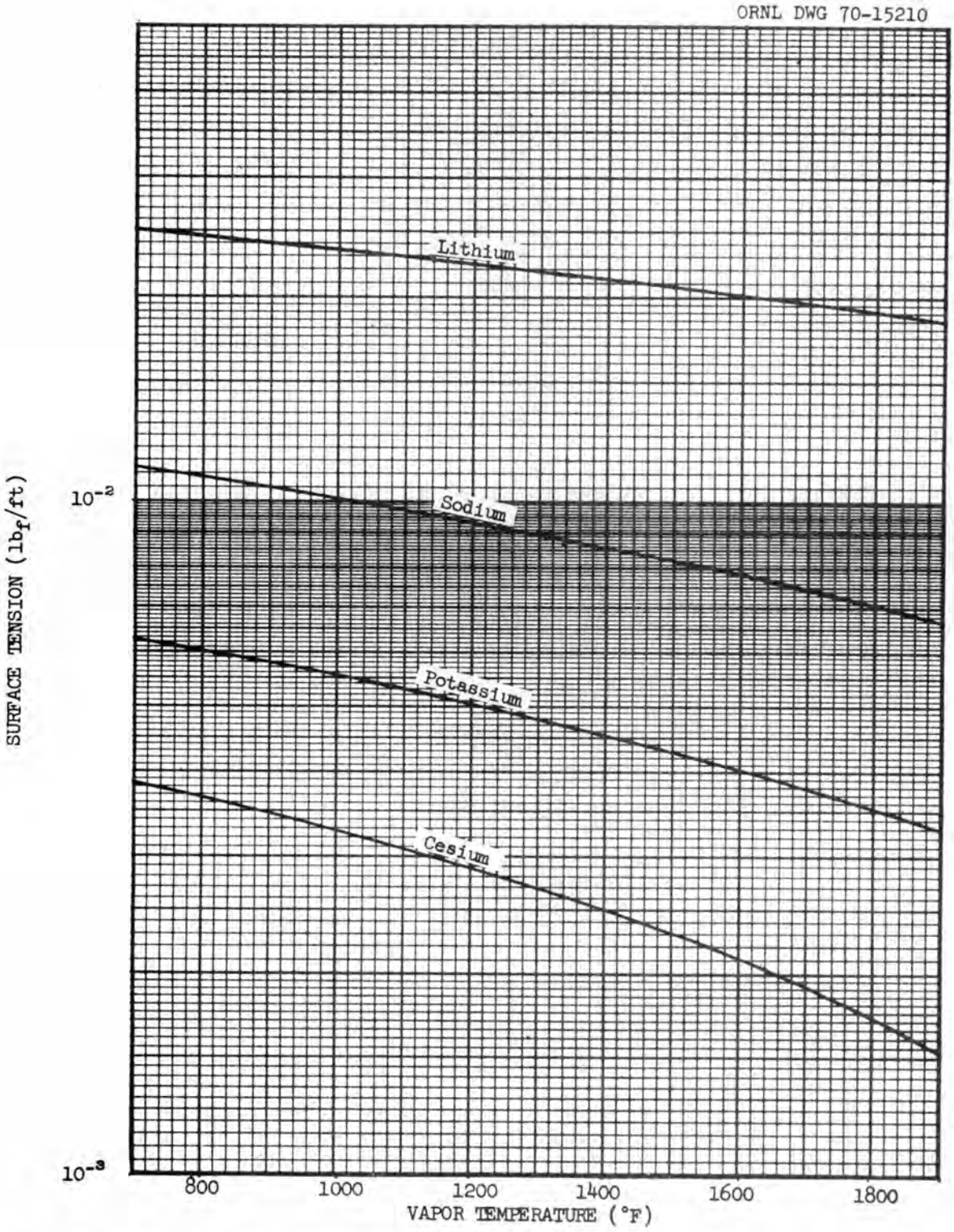

Fig. 2. Surface Tensions for Cesium, Potassium, Sodium, and Lithium as Functions of Vapor Temperature.

ORNL DWG 70-15211

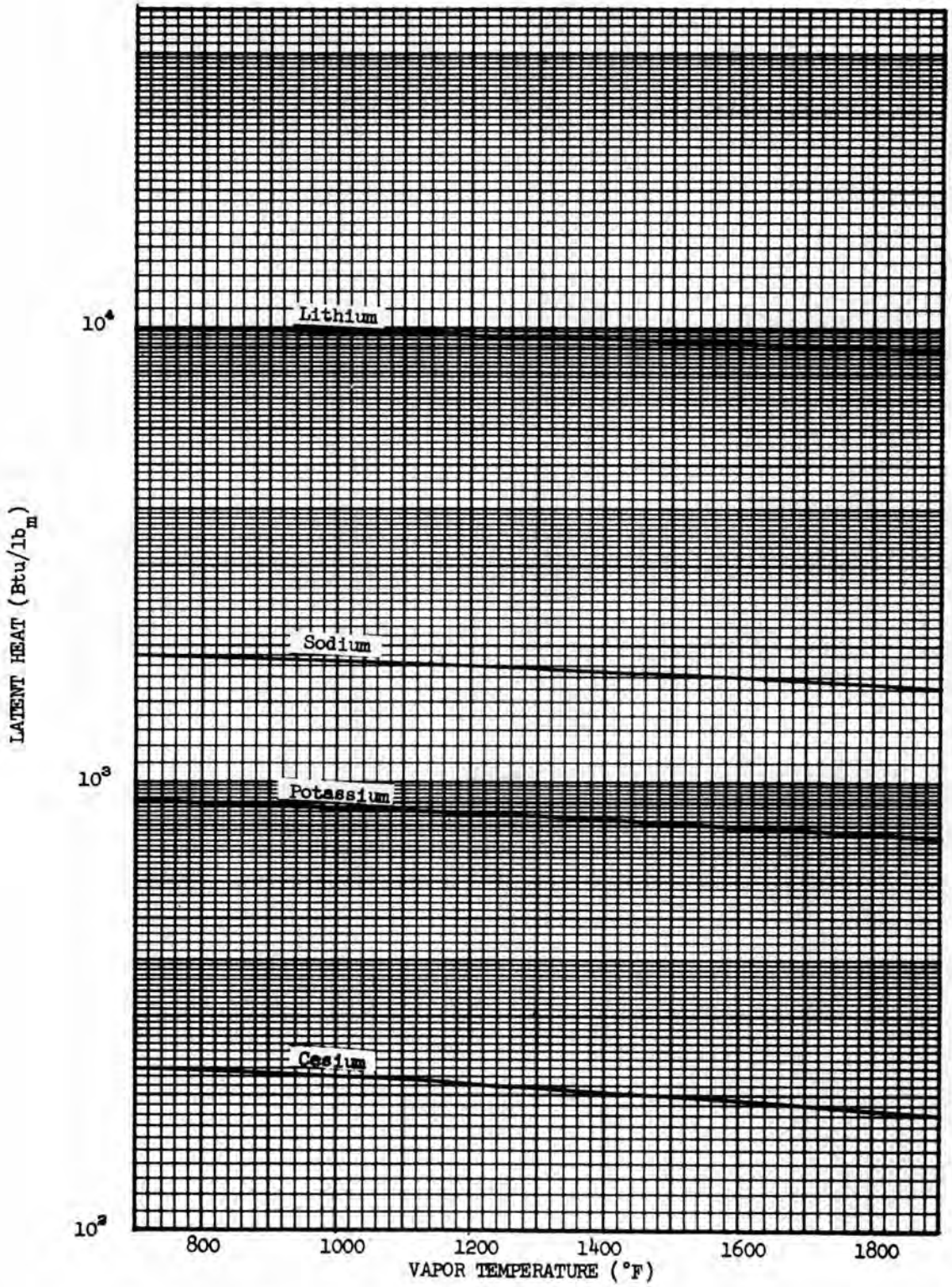

Fig. 3. Latent Heats for Cesium, Potassium, Sodium, and Lithium as Functions of Vapor Temperature.

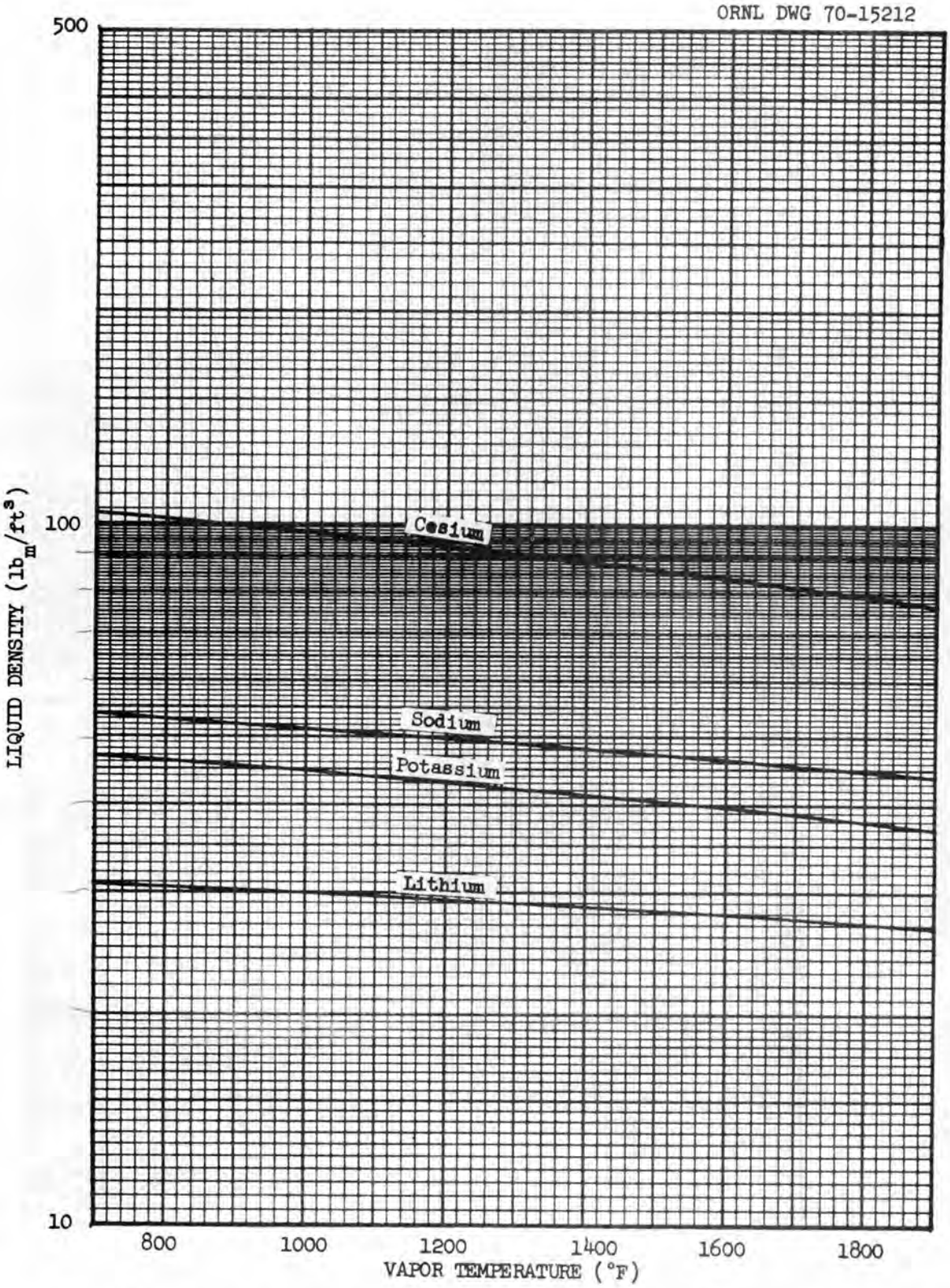

Fig. 4. Liquid Densities for Cesium, Potassium, Sodium, and Lithium as Functions of Vapor Temperature.

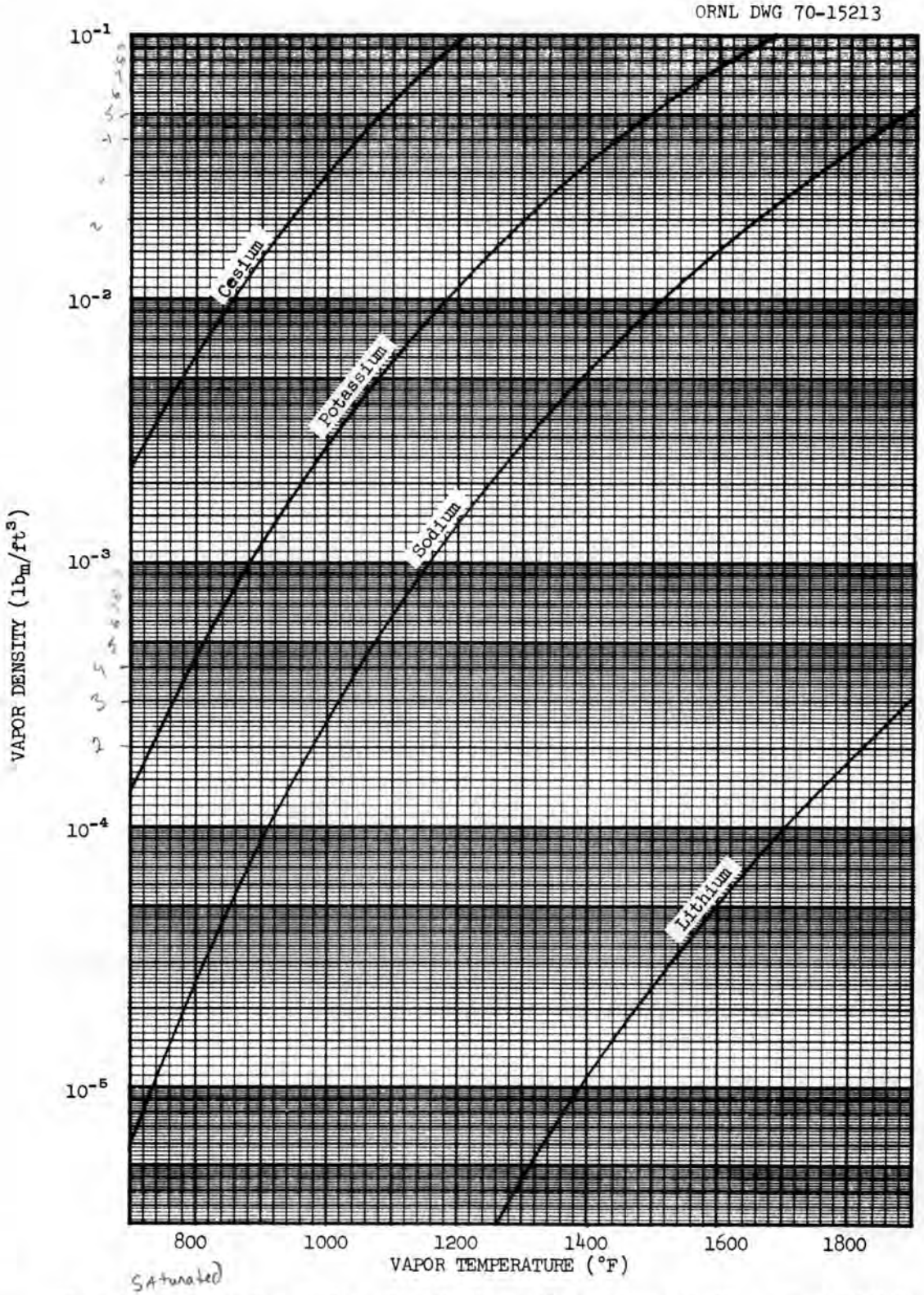

Fig. 5. Saturated Vapor Densities for Cesium, Potassium, Sodium, and Lithium as Functions of Vapor Temperature.

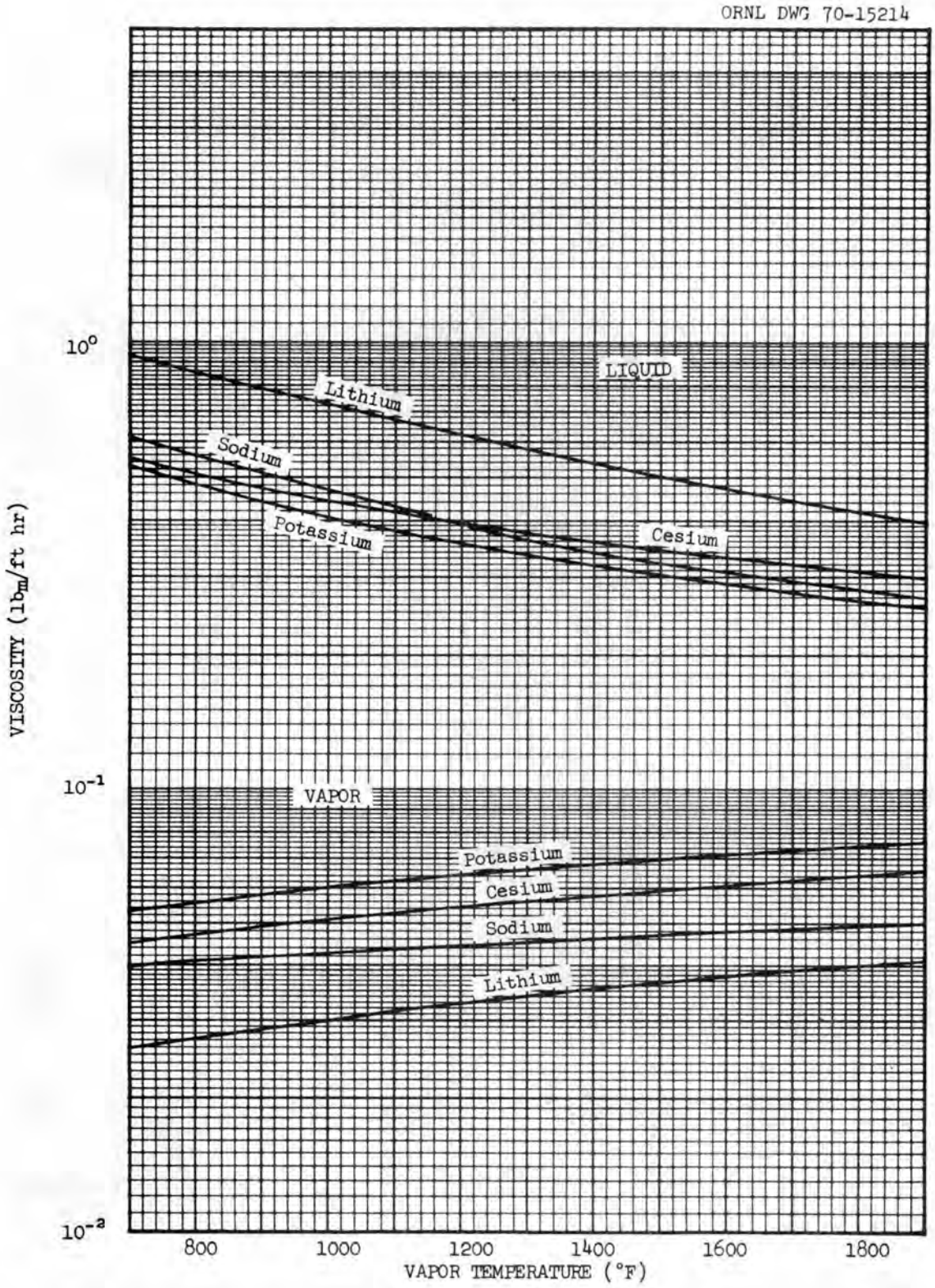

Fig. 6. Liquid and Vapor Viscosities for Cesium, Potassium, Sodium, and Lithium as Functions of Vapor Temperature.

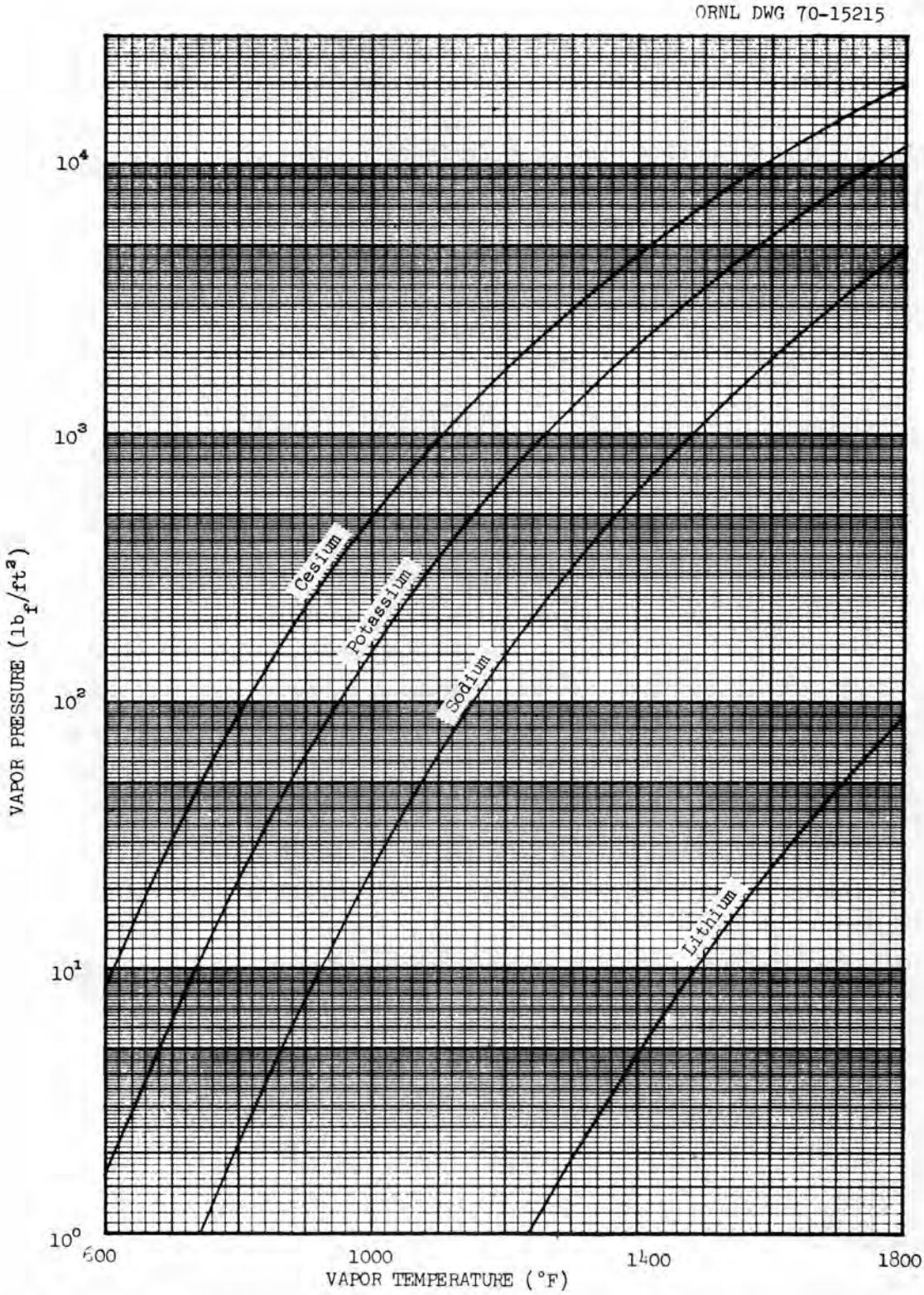

Fig. 7. Vapor Pressure of Cesium, Potassium, Sodium, and Lithium as Functions of Vapor Temperature.

required, high liquid density can be a mixed blessing. With the condenser at the bottom, the liquid static head opposes the capillary driving force, so that, depending on orientation, the heat pipe may be drastically reduced in capacity or completely inoperable. On the other hand, with the condenser above the evaporator, it may be necessary to operate the pipe at some minimum power output in order to retain liquid in the evaporator capillary structure against the liquid static head.

Viscosity

A low viscosity in both the liquid and vapor phases is desirable in order to produce a minimum resistance to fluid circulation in the heat pipe.

Vapor Pressure

The choice of a heat pipe working fluid, as influenced by the vapor pressure, depends on the required operating temperature. In the vicinity of this temperature, the vapor pressure-temperature curve should have a relatively steep slope in order that the pressure difference between evaporator and condenser required in order to maintain vapor flow should not produce a large temperature gradient. A low vapor pressure at the operating temperature implies a low vapor density with consequent high vapor velocity, high Mach number operation, and again, large temperature gradients along the heat pipe. Pressure, however, should not be so high that pressure-induced stresses are a problem, since thin walls are desirable both for efficient radial heat transfer and for low weight.

CAPILLARY STRUCTURES

Despite the multitude of capillary structures, or wicks, used thus far in heat pipe designs, such structures divide naturally into two basic types, simple and composite. Figure 8 illustrates some examples of each type of structure.

ORNL DWG 70-15216

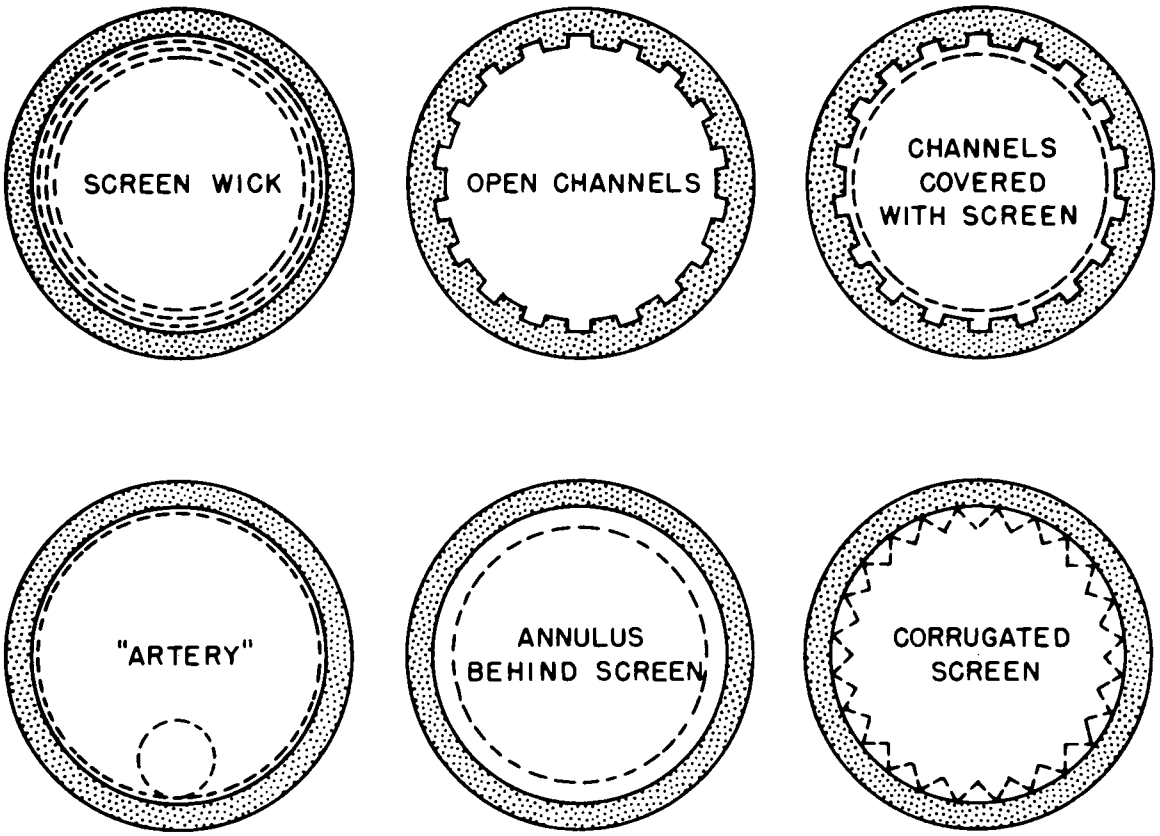

Fig. 8. Some Examples of Heat Pipe Capillary Structures.

The simple type, exemplified by the screen wick and open longitudinal channels, combines, in a single structure, the disparate functions of providing a liquid-return path and producing the required capillary driving force. In general, because of the conflicting requirements, improvement in one of these functions cannot be attained in the simple structure without a worsening of the other.

In the composite structure, such as the "artery" and the screened annulus, the two above functions are largely separated. Ideally, they are completely divorced. Thus, the magnitudes of the capillary force and resistance of the liquid-return path can be specified independently, subject primarily to the constraints of fabricability.

Screen Wicks

Historically, the screen, or mesh, wick was the first capillary structure to be employed in a heat pipe (except for some initial qualitative experiments[1] with water, in which a porous Alundum tube was used). The simple screen wick has the advantage of being relatively simple to fabricate and is made from fine mesh screen, which is readily available in a variety of materials. One method of constructing such a wick is to roll a number of layers of fine mesh screen into a cylindrical tube, which is then inserted into the container and compressed against the container wall by, say, pushing a steel ball through the entire assembly.

Because the simple screen wick has an inherently high resistance to liquid flow it does not permit attainment of high axial heat fluxes. In order to circumvent this difficulty, the composite screen wick might be employed. In the composite wick, layers of relatively coarse mesh screen, adjacent to the container wall, are used to provide a liquid-return path and one or more layers of fine mesh screen, at the vapor liquid interface, are used to provide capillary driving force. As might be surmised, this construction considerably complicates fabrication of the screen wick.

While very careful control of the fabrication process would undoubtedly yield screen wicks, of either of the simple or composite variety, having reproducible flow and capillary characteristics, there do not appear to be sufficient data, at this time, to allow fabrication to preset specifications.

Longitudinal Channels

An alternate form of capillary structure consists of many longitudinal channels evenly spaced around the inside circumference of the container. These channels may be either integral with the container wall[5] or be formed by an insert consisting of axial strips held together on the inside by rings.[18] In the latter case, the capillaries are formed by the interval between the strips.

A cross section through the integral type of structure is shown in Fig. 8. The most commonly used method of fabrication seems to be the milling of the appropriate number of rectangular slots in a flat sheet of the heat pipe material, followed by rolling the sheet into a tube and closing by means of a longitudinal weld. This type of structure is very stable and the capillary size can be controlled quite well. The weld, however, presents a possible weak point in the structure.

It is of interest to note that, in approximately 270,000 hours of heat pipe operation by RCA,[19] only two heat pipe failures were reported, both of these being weld failures at roughly 10,000 hours operating time for each pipe.

The capillary insert described in Ref. 18 is fabricated by spinning a seamless tube over a specially shaped mandrel, machining to a uniform diameter, milling axial capillary slots, and chemical dissolving of the mandrel as a final step. Since all machining is done on the outside of the tube, it should be possible to make long inserts of relatively small diameter with good control of the capillary size. With this type of capillary structure, one is able to use a seamless tube for the heat pipe container, an obvious advantage.

Other fabrication techniques, which could be or have been used, include broaching, extrusion (used with rather limited success[20]), and vapor deposition.[21]

The pressure difference across a liquid-vapor interface is given by

$$\Delta P = \sigma\left(\frac{1}{r_1} + \frac{1}{r_2}\right) \tag{1}$$

where σ is the surface tension, and r_1 and r_2 are the principal radii of curvature of the interface. (Appendix B contains a listing of nomenclature.)

In the open channels described above, the axial radius of curvature is essentially infinite and contributes nothing to the pressure difference, while the other principal radius becomes the half-width of the capillary channel. Thus, equation one reduces to

$$\Delta P = \frac{\sigma}{r_c} \tag{2}$$

where r_c is the channel half-width.

If the channels are covered with a screen whose wire-to-wire spacing is equal to the channel half-width, the principal radii of curvature become equal to each other and to the channel half-width. Equation one then reduces to

$$\Delta P = \frac{2\sigma}{r_c} \tag{3}$$

and the available capillary driving force becomes double that from the open channels. The beneficial effect of this relatively simple modification is shown in Fig. 9, the data for which come from Ref. 5.

Artery

The "artery" heat pipe separates the function of returning the liquid to the evaporator from that of producing a capillary driving force. This is accomplished by combining a tube, whose sole function is that of liquid return to the evaporator, with, say, a screen wick, which distributes the liquid peripherally and provides the capillary forces. The tube, of fine screen, communicates intimately with the wick throughout its length.

Moritz[22] has described an interesting variation on the artery in which a screw thread (essentially, a continuous peripheral capillary) machined into the pipe wall serves as the wick. The effect of thread profile on heat pipe capacity has not been investigated. A variety of configurations (nine, in all) is shown in Ref. 22.

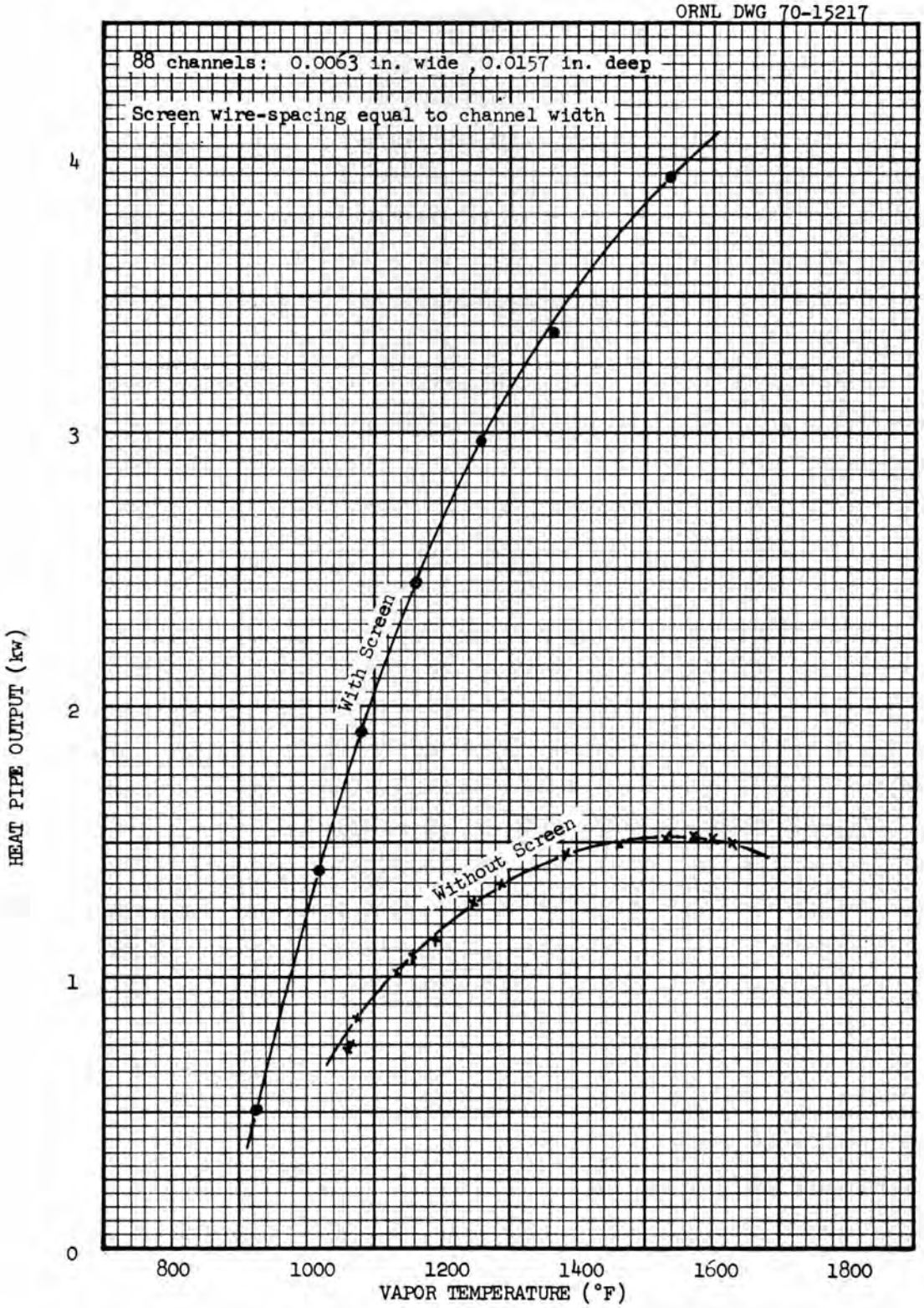

Fig. 9. Effect of Channel Screen Cover on Axial Heat Flow in a Sodium Heat Pipe.

Annulus

The "annulus" type of construction,[4] wherein a porous tube is inserted into a slightly larger seamless container, offers perhaps the ultimate in reduction of resistance to fluid flow. The fine porosity inner-tube, which forms a circular passage for the vapor flow, effectively separates the vapor and liquid streams, thus minimizing interaction between the two flows. Further, the gap between the inner and outer tubes provides a completely unobstructed path for the liquid return.

With the annulus full of liquid and the porous tube closed at each end (this latter point is important), the capillary forces are dependent only on the effective pore radius of the tube openings at the vapor-liquid interface. Thus, the capillary driving force can be determined independently from the resistance of the liquid return path.

Kemme[4] has described a method for producing suitable rigid tubes with fine, reproducible porosity and smooth walls. Multiple layers of fine-mesh screen are wrapped on a copper tube mandrel and placed in another copper tube. The entire assembly is then drawn down through a die in order to compress the screen layers. Chemical dissolution of the copper is followed by heating in vacuum to about 1800°F to bond the layers.

Pore-size measurements, made by submerging the tubes in well-wetting liquids, internally pressurizing with gas, and noting the pressure difference at which gas bubbles broke through, yielded effective pore sizes of about 19 microns. This was about half the size of the openings in the original 400-mesh screen. The effective pore sizes were obtained from

$$r_c = \frac{2\sigma}{\Delta P}, \tag{4}$$

which is simply Equation 3, rearranged.

Busse et al[18] mentioned the use of a perforated tube insert with an annular gap. However, the capillary was said to be formed by the gap between the insert and the container. This would imply a low performance, resulting either from low capillary force (large gap) or high liquid flow resistance (small gap). A porous tungsten insert was also mentioned in passing. Details, however, were minimal and no data were quoted.

The annulus shares with the artery the potential disadvantage of sensitivity to emptying of the liquid channel during vertical operation under gravity. This could come about if a long heat pipe were subjected to an axial shock or a vapor bubble should form in the annulus. This problem is minimized, of course, if the pipe is operated in the horizontal position or in a gravity-free environment.

Other Structures

The above discussion does not exhaust, by any means, the usable forms of capillary structures, which seem to be limited only by the ingenuity of the designer. For instance, porous sprayed coatings, matted fibers, and packed spherical beads have been used. However, it is felt that such structures represent, primarily, variations on the above themes and will not be discussed here.

OPERATING EXPERIENCE

As a two-phase, refluxing system, the heat pipe is heir to all the ills of such systems, including mass transfer and corrosion. However, with careful attention to materials compatibility and proper loading procedures, heat pipe lifetimes of as high as 28,000 to 37,000 hrs have been reported without measured decrease in heat-transfer capacity or significant corrosion. Table 1 summarizes the readily obtainable lifetime data as of August 1970.

Busse[23] has reported on some lifetime tests done at Brown-Boveri and at the Ispra Euratom Research Center. Brown-Boveri operated a niobium-zirconium heat pipe with sodium at 1560°F for over 16,000 hrs and a similar heat pipe with cesium for more than 5,000 hrs without signs of deterioration. At Ispra, 1000-hr tests with niobium-zirconium heat pipes were made using cesium and sodium at 1830 and 2010°F, respectively. It was reported that no corrosion of any type could be detected.

Screening tests performed at Ispra at approximately 2900°F turned up only two combinations of materials that showed promise for a 10,000-hr

Table 1. Summary of Heat Pipe Operating Experience

Working Fluid	Container Material	Operating Temperature (°F)	Power Transferred (kw)	Operating Life (hr)	Status
			RCA		
Acetone	304SS	50	.01	9,140	Continuing.*
Water	Copper	300	.19	20,420	Continuing.
Water	Copper	210	.25	19,490	Continuing.
Water	Copper	175	.04	21,360	Continuing.
Acetone	Aluminum	230	.07	1,700	Terminated. Some performance degradation.
Acetone	304 SS	190	.03	14,390	Continuing.
Mercury	304 SS	645	.36	27,860	Continuing.
Potassium	Nickel	1110	1.75	36,605	Continuing.
Potassium	Nickel	1110	1.20	10,000	Terminated under contract.
Potassium	Nickel	1110	1.75	6,000	Terminated under contract. Two pipes.
Sodium	Hastelloy X	1320	.20	33,100	Continuing.
Sodium	Hastelloy X	1320	.20	8,000	Terminated. Pipe shipped to JPL.
Sodium	316 SS	1420	.30	11,860	Failed. Small pinhole in evaporator.
Sodium	Nickel	1470	.20	13,735	Terminated. Equipment needed.
Sodium	304 SS	1470	.30	12,760	Terminated. Equipment needed.
Lithium	TZM	2730	2.00	10,400	Weld failure in end cap.
Lithium	TZM	2730	2.00	9,800	Weld failure in end cap.
			Los Alamos		
Water	347 SS	195	.1	15,000	Terminated.
Mercury	347 SS	625	.1	10,000	Terminated.
Cesium	Titanium	750	.5	2,000	Terminated.
Potassium	347 SS	930	.5	6,500	Terminated.
Sodium	347 SS	1380	1.2	1,500	Terminated.
Lithium	Niobium-Zirconium	2010	1.0	4,300	Terminated.
Lithium	Niobium-Zirconium	2010	1.5	2,000	Terminated.
Silver	Tungsten	3450	1.5	1,000	Terminated.
			Euratom CCR, Ispra		
Cesium	Niobium-Zirconium	1830	?	1,000	Terminated.
Sodium	Niobium-Zirconium	2010	?	1,000	Terminated.
			Brown-Boveri		
Cesium	Niobium-Zirconium	1560	.5	5,000	?
Sodium	Niobium-Zirconium	1560	.5	16,000+	?

*Continuing tests show no performance degradation. The same holds for terminated tests except where noted.

Sources:

RCA. Ref. 19, Table 1. Updated to August 1970; personal communication from G. Y. Eastman.

Los Alamos. Personal communication from J. E. Kemme, August 1970.

Euratom and Brown-Boveri. Ref. 23

lifetime. These were lithium and lead in tungsten. It was stated that all the ductile heat pipes showed "relatively strong corrosion."

In the United States, Eastman[19] has reported on a variety of fluid- and pipe-material combinations on which a total of over 270,000 hrs of operation has been accumulated. The fluid-material combinations ranged from water in copper to lithium in TZM and the corresponding operating temperatures from approximately 180°F to over 2730°F. Operating lifetimes ranged from 1700 to over 36,600 hrs.

Several of the liquid-metal-containing heat pipes are worthy of note. A potassium in nickel combination was operated at approximately 1110°F for over 36,600 hrs; as of August 1970, this test was continuing. Similarly, a sodium in Hastelloy-X combination had accumulated more than 33,000 hrs of operation at approximately 1320°F. This test was also continuing. Two lithium-in-TZM heat pipes were operated at over 2730°F for 9800 and 10,400 hrs. These tests were terminated because of weld failures. The operating lives quoted are said to be for continuous operation without any measured decrease in heat-transfer capacity.

Five heat pipes, using the Los Alamos porous-tube insert described above, recently completed endurance tests of approximately 6000 hrs each. The heat pipes were made of nickel with potassium as a working fluid at approximately 1100°F. These units were built and operated by RCA and Sandia, and the post-test metallurgical examination was carried out at ORNL.[24] Examination showed a small amount of oxygen attack, apparently as a consequence of contamination during the original filling operation. Performance was not adversely affected by this corrosion, and there was no difficulty with clogging of the wick structure as a consequence of mass transfer deposits.

Deverall and Kemme[25] have reported the successful operation of a silver in tantalum-5% tungsten heat pipe at temperatures up to 3630°F. Cotter et al[21] have reported further on this heat pipe after operation for 100 hrs at 3450°F. Mass transfer of tantalum was observed, with the solubility in silver being estimated as of on the order of 10 ppm. Substitution of a tungsten screen for the tantalum screen appeared to improve matters substantially. The tungsten screen appeared unchanged after operation at 3450°F for approximately 100 hrs. Lesser deposits from the evaporator

appeared to be dissolved tantalum from the container wall. Results were sufficiently encouraging that vapor-deposited tungsten containers were obtained for further tests. As indicated in Table 1, about 1000 hrs have been accumulated in intermittent testing.

At the other end of the temperature spectrum for liquid-metal heat pipes, Eastman[19] has reported operation of a mercury in stainless steel heat pipe at approximately 645°F for a period of 28,000 hrs, with the test continuing. As noted previously, operating lives are for undiminished performance. Deverall[26] has reported a 10,000-hr life test on a similar heat pipe. Small amounts of magnesium and titanium were added to the mercury to improve wettability and to inhibit corrosion, respectively. Post-test sectioning of the heat pipe showed both the wick structure and the tube wall to be in good condition. However, some corrosion and mass transfer had occurred. The principal corrosion effect appeared to be a stress corrosion occurring at the crossover points of the screen wires, probably resulting from compression of the screen during assembly of the heat pipe. Size and porosity of the mass-transfer deposits were such that heat-pipe operation would not be affected.

It is evident from the foregoing experience that, with adequate attention to the materials compatibility problem, heat-pipe assembly, and proper loading, the heat pipe is capable of long reliable service.

HEAT TRANSPORT LIMITATIONS

Since the heat pipe is a two-phase flow system, with the liquid and vapor phases closely coupled, its operation is subject to certain limitations imposed by compressibility effects and vapor-liquid shear interactions. These limitations include sonic flow at the evaporator exit, possible difficulties in startup from ambient to operating conditions, possible entrainment of liquid in the rapidly moving vapor, and the ability of the generated capillary forces to overcome the liquid and vapor flow resistances.

Sonic Flow

The axial heat flux at the evaporator exit of an operating heat pipe is given by

$$\frac{Q}{A} = \rho_v \, V \, h_{fg} \quad , \tag{5}$$

where $\frac{Q}{A}$ = the axial heat flux at the evaporator exit, ρ_v = the average vapor density at the exit, V = the average axial vapor velocity at the exit, and h_{fg} = the latent heat of vaporization. This heat flux attains its upper limit when the average velocity of the vapor leaving the evaporator becomes sonic. This condition can be reached if the operating temperature is reduced sufficiently while maintaining heat input to the evaporator constant. The resulting decrease in vapor density then causes the vapor velocity to increase until it becomes sonic. The situation is quite analogous to (but not the same as!) attainment of the sonic condition at the throat of a convergent, constant mass flow nozzle as the exit pressure is reduced.

Shapiro[27] has developed an analysis for the one-dimensional, steady, continuous flow of a semiperfect gas. The various physical equations and definitions, such as the equation of state, the Mach number, and the momentum equation, are expressed in logarithmic differential form. The resulting set of simultaneous equations is linear in the logarithmic differentials, thus allowing easy separation of the physical variables.

The results of this analysis, for constant molecular weight and specific heat, are presented in Ref. 27 as a set of influence coefficients. The influence coefficients, which are simply the coefficients of the independent variables, are so called since they indicate the influence of each of the independent variables on each of the dependent quantities. The influence coefficients may be used to derive relationships between each of the dependent variables and the Mach number for simple flows, where a simple flow is defined as one in which all but one of the independent differentials are zero. These relationships may be integrated analytically for each of the simple flows. The resulting formulas are summarized in Table 8.3 of Ref. 27.

It is convenient to express the sonic heat flux in terms of vapor conditions at the evaporator inlet, since these are more readily determined

than exit conditions. With the use of the appropriate terms from Table 8.3 of Ref. 27, Equation 5 for sonic conditions can be transformed to

$$\frac{Q_s}{A} = \frac{\rho_v V_s h_{fg}}{\sqrt{2(k+1)}} \tag{6}$$

where the s subscript indicates sonic conditions and k = the ratio of the specific heats of the vapor. All properties are evaluated at the evaporator inlet temperature.

Sonic heat fluxes calculated by means of Equation 6 are shown in Fig. 10 for cesium, potassium, sodium, and lithium as functions of the evaporator inlet temperature. For these calculations, k was assumed to be 1.667, a value appropriate to a monatomic vapor. Experimental curves obtained from Ref. 4 are shown superimposed on the calculated curves for the first three alkali metals. Data were not available for lithium.

As noted by Kemme[4], complete agreement between the experimental and calculated curves was not obtained. Kemme speculated that small amounts of noncondensable gases or the failure, in the calculations, to account for the presence of dimers in the vapor might be responsible for the discrepancies. However, Kemme's calculated curves lie consistently above the experimental data. This is observed not to be the case in Fig. 10. One might also speculate, then, that the differences could be ascribed to variations in the fluid properties used in the calculations. In any event, the agreement between calculation and experiment seems quite good.

Kemme[4] has determined the sonic and subsonic performance of both a cesium and a sodium heat pipe. These data provide a further check on the ability of the one-dimensional compressible flow equations to predict the compressibility-limited performance of heat pipes. Figure 11 shows Kemme's data plotted in terms of evaporator pressure ratio as a function of the fraction of sonic heat transport, where the sonic heat-transfer rate, Q_s/A, is defined by Equation 6.

From Table 8.3 of Ref. 27, one may obtain expressions for the ratio of the local vapor pressure to that at sonic conditions in terms of the local Mach number. Taking the ratio of these expressions, written for inlet and exit conditions in the evaporator, one obtains the evaporator pressure ratio as

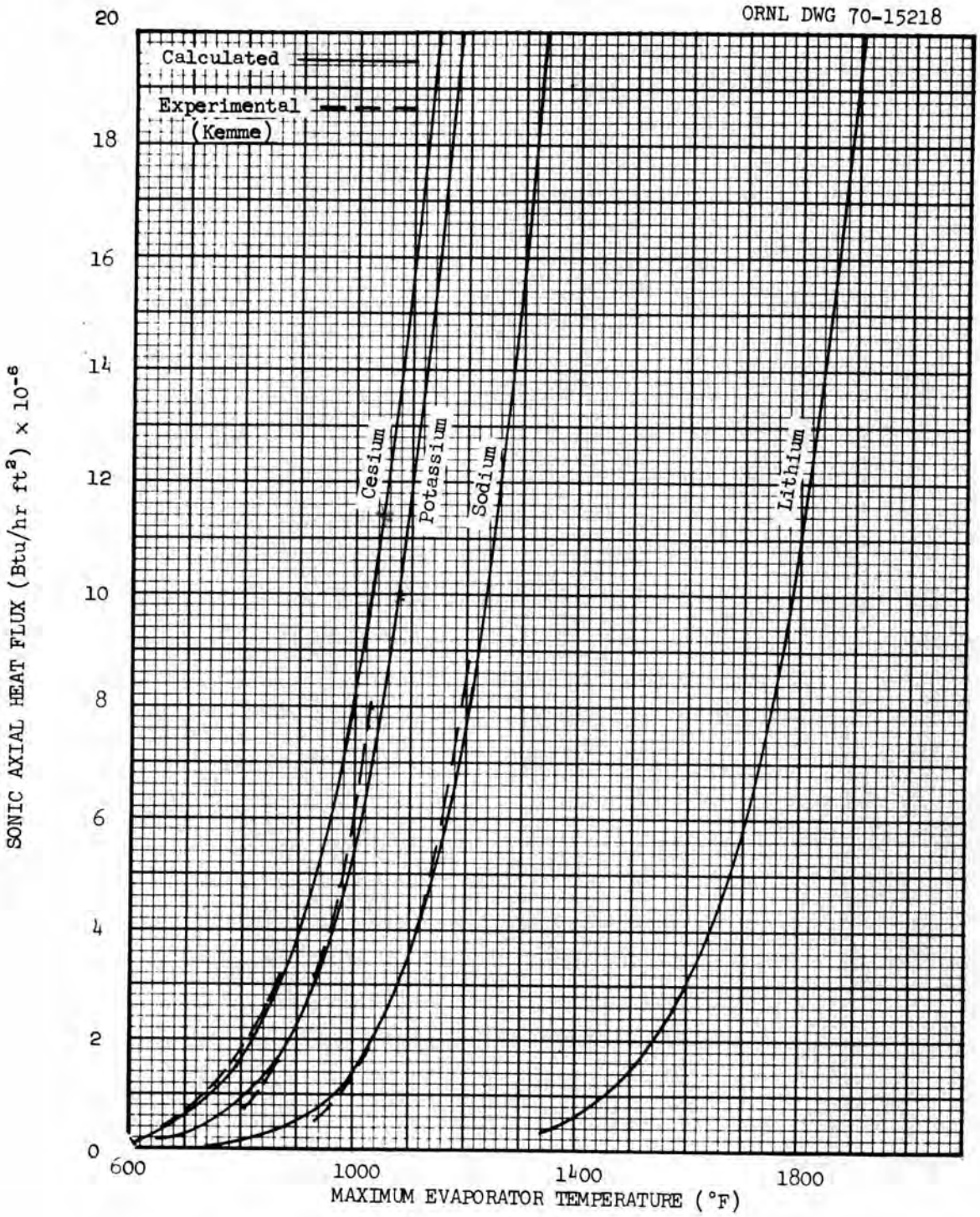

Fig. 10. Comparison of Calculated and Experimental Sonic Limits on Axial Heat Flow for Cesium, Potassium, and Sodium Heat Pipes. Calculated values only for lithium.

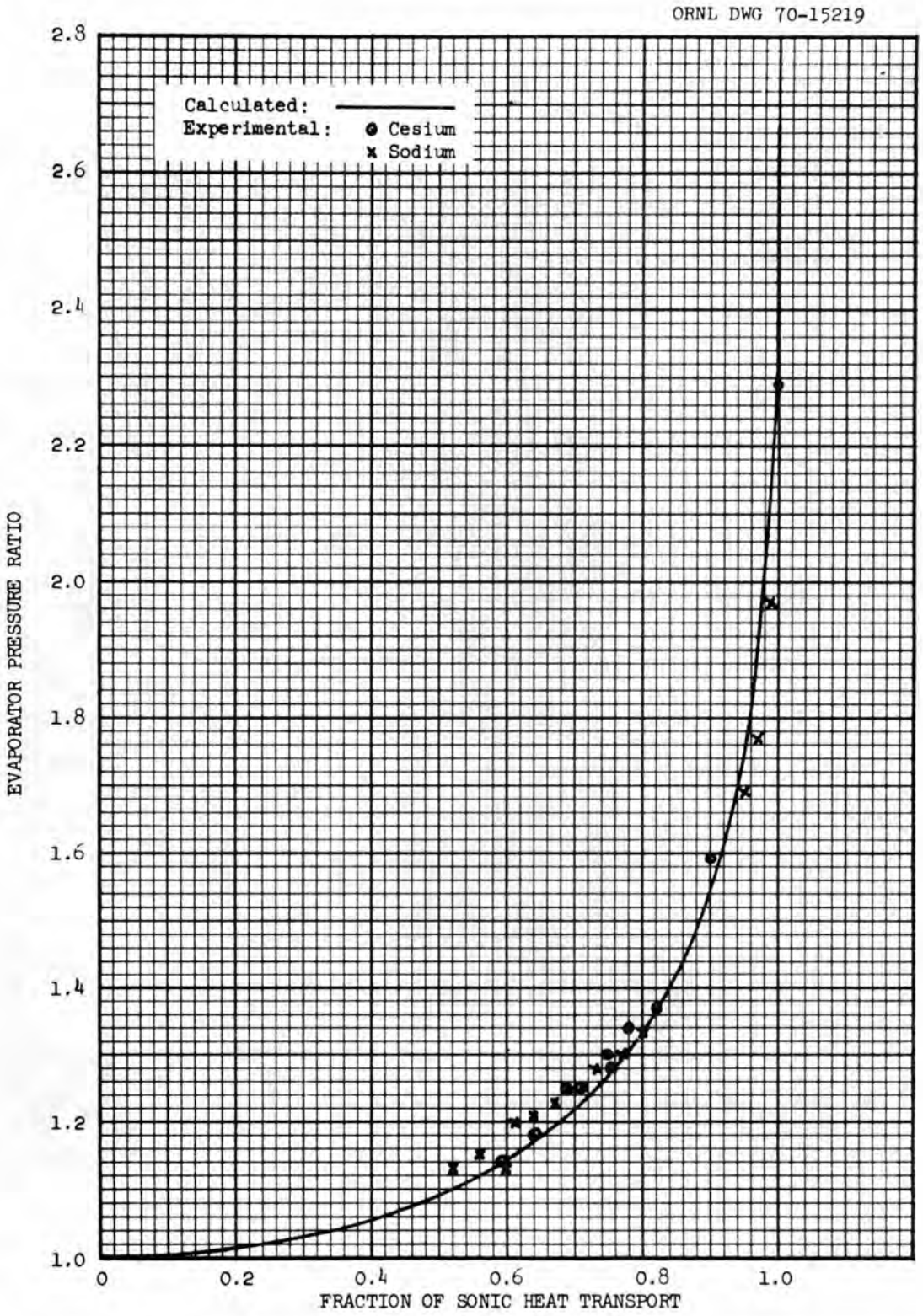

Fig. 11. Evaporator Pressure Ratio as a Function of Sonic Heat Transport Fraction. Comparison of calculated values with experimental data for cesium and sodium.

$$\frac{P_1}{P_2} = 1 + kM^2 \tag{7}$$

where P_1 and P_2 are the evaporator inlet and exit pressures, respectively, and M is the exit Mach number. The fraction of sonic heat transport may be determined directly from Table 8.3 as

$$\frac{Q}{Q_s} = \frac{M\sqrt{2\ (1+k)\ (1+\frac{k-1}{2}M^2)}}{1 + kM^2} \tag{8}$$

where Q is the heat transport at the exit Mach number, M. A calculated curve, determined from Equations 7 and 8, is shown superimposed on the experimental data in Fig. 11. The agreement between calculation and experiment is seen to be excellent. For a Mach number of one, the evaporator pressure ratio can be determined from Equation 7 to be 2.667 for a monatomic vapor. Note that the relationship shown in Fig. 11 is independent of any fluid property except specific heat ratio. Hence, to the extent that this same ratio is independent of temperature, the function of Fig. 11 does not depend on either operating temperature level or power output of the heat pipe.

Although the heat pipe is commonly thought of as an essentially isothermal device, large temperature drops occur in the evaporator when the heat pipe is operated at or near a sonic limit. This effect is shown in Fig. 12 where calculated evaporator temperature drops at sonic flow have been plotted as a function of maximum evaporator temperature for cesium, potassium, sodium, and lithium. The maximum evaporator temperature occurs at the evaporator inlet. These curves can be obtained graphically from the vapor pressure curves in Fig. 7. Having determined inlet vapor pressure from the given inlet temperature, one simply divides the inlet pressure by the appropriate pressure ratio (in this case, 2.667) to obtain the exit pressure and, hence, the exit temperature from the curves in Fig. 7.

It is obvious from Fig. 12 that very large temperature drops occur in the evaporator when a heat pipe is operated with sonic flow at the evaporator exit. It can also be seen that this temperature drop increases with operating temperature. However, the sonic axial heat flux is also greater,

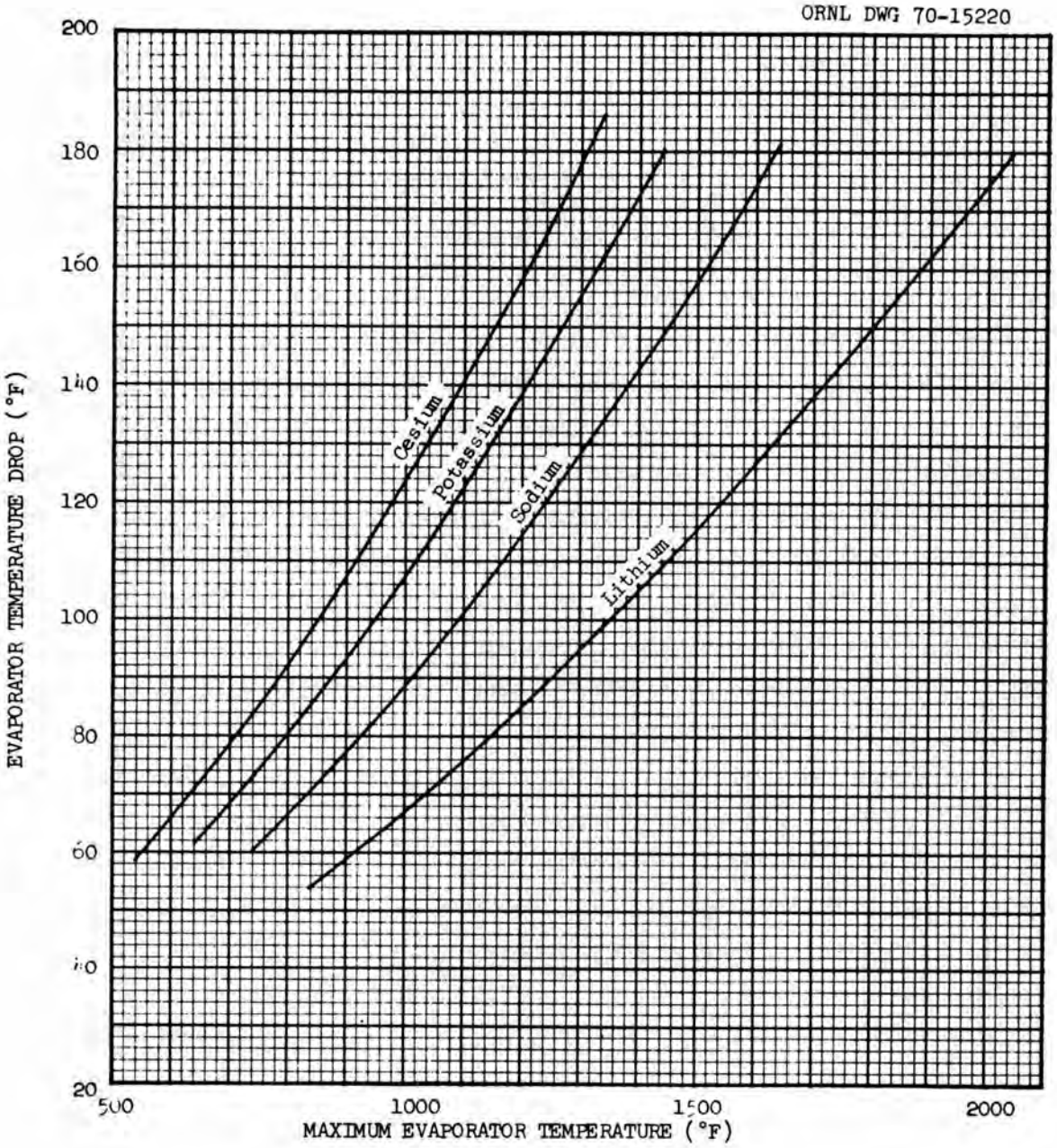

Fig. 12. Calculated Evaporator Temperature Drop at Sonic Flow as a Function of Maximum Evaporator Temperature for Cesium, Potassium, Sodium, and Lithium.

as can be seen from Fig. 10. As will be shown by the following example, the conclusion to be drawn is that heat pipe operation at high vapor density and, thus, high temperature is preferable to operation at high vapor velocity.

Consider a potassium heat pipe with an inlet temperature of 960°F. The corresponding sonic-limited heat flux is 3.9×10^6 and the evaporator temperature drop is 102°F. If we reduce the evaporator pressure ratio to, say 1.1, a value commensurate with negligible compressibility effects, the corresponding fraction of sonic heat transport becomes 0.52, as can be seen from Fig. 11. The corresponding sonic-limited heat flux now becomes 7.5×10^6 and the evaporator inlet temperature, 1040°F. For the given pressure ratio, the exit temperature is now 1030°F, for an overall evaporator temperature drop of only 10°F. Thus, the evaporator temperature drop has been reduced by a factor of 10 for only a modest increase in maximum temperature.

Startup

The heat pipes of interest in the present application must ordinarily be brought from, say, ambient temperature and zero heat flux to a rather high operating temperature and heat flux. If a given heat pipe is capable of nearly isothermal operation at a particular design temperature and heat flux, startup always may be accomplished by first heating uniformly to the design temperature and then increasing the heat flux to the design value while holding the temperature constant. However, this technique is rarely convenient and quite likely to be impossible in practice. It is the purpose of this section to review, briefly, some of the phenomena inhibiting startup and, at least, to indicate means for circumventing them.

The first of the two categories into which startup failures may be grouped results from exceeding the superheating limit of the working fluid during startup. In this failure mode, the evaporator dries out due to boiling in the capillary structure and overheating of the evaporator then occurs. However, this type of failure is not likely to occur where the heat pipe is known to be operating below the superheating limit at design

conditions. Inasmuch as the superheating limit increases with decreasing temperature in the temperature range of interest, it would be sufficient to maintain the startup heat flux at or below the design heat flux at all times.

The second category of startup failures comprises all those mechanisms that result in evaporator dryout because of insufficient return of working fluid to the evaporator. For example, if the working flud has a high vapor pressure at the melting point, startup may be impossible because of complete transfer of the working fluid by sublimation from the evaporator and deposition as solid in the condenser. Busse[18] has reported on a heat pipe filled with magnesium, having a vapor pressure of 2.8 mm Hg at the melting point, which proved impossible to start up without preheating. Fortunately, the alkali metals are not subject to this particular limitation.

Where a substantial portion of the liquid surface is exposed to high-velocity vapor flow, as would occur with unprotected longitudinal capillary grooves, for example, the liquid return may be substantially retarded by the interfacial shear occurring between the countercurrent vapor and liquid streams. In addition, the dynamic instability that occurs at the vapor-liquid interface may result in entrainment of liquid droplets in the vapor flow. Kemme[3] found that a sodium heat pipe with unprotected longitudinal grooves was difficult to start. When the grooves were widened in order to reduce liquid pressure drop, the pipe could not be started at all. Covering the channels with a screen, thus reducing the interaction between the two streams, reduced the problems of startup in the first case and made startup possible in the second.

Cotter[28] has presented a theoretical analysis of the transient behavior of heat pipes during startup. Although detailed experimental confirmation is lacking, the available data do appear to confirm the general conclusions of the theory. It appears that, in the absence of other constraints, the startup difficulties may be overcome by proper design or a reasonable startup program.

Entrainment

In a cylindrical heat pipe, vapor and liquid move in opposite directions, often in fairly intimate contact. One effect of the resulting interaction is an increase in the liquid pressure drop. More importantly, this interaction may become sufficient to tear liquid from the surface and entrain it as droplets in the vapor stream. Since the entrained liquid must be accommodated by the liquid return system, a point is eventually reached where the increased load cannot be handled. At this point, the entrainment limit, sufficient liquid is not being returned to the evaporator and overheating occurs.

From the linear theory of the dynamic instability which causes entrainment[29], the condition for a stationary wave profile on the liquid surface (incipient instability) is that the inertial energy of the vapor stream should just equal the surface energy of liquid. The ratio of these energies is defined to be the Weber number, We. The condition for incipient instability then is

$$We = \frac{\rho_v V^2/g_c}{\sigma/z} = 1 \tag{9}$$

where σ equals the surface tension of the liquid in contact with its vapor and z equals a characteristic dimension of the surface. Rewritten in terms of axial heat flux, Equation 9 becomes

$$\frac{Q}{A} = h_{fg}\sqrt{\frac{g_c \rho_v \sigma}{z}} \tag{10}$$

Unfortunately, beyond indicating the form of the expression for the entrainment-limited heat pipe output, stability theory is of little assistance. For instance, while z is related to the wave length of the disturbance at the liquid vapor interface as instability sets in, it is not at all clear just what wave length should be used where, say, a fine mesh screen is interposed between the two phases. One might hypothesize that the wire spacing or, perhaps, the wire diameter would be the appropriate dimension to use. Recourse must, therefore, be had to experiment in order to settle this question.

Kemme[3] has measured the entrainment-limited heat flux of a sodium heat pipe. The onset of entrainment was detected by listening for the sound of liquid drops impinging on the end of the condenser. The composite wick of this heat pipe consisted of 39 channels, 0.75 mm square, covered with a fine mesh screen. The screen consisted of 46 μ diameter wires spaced on 56 μ centers, giving a screen opening of 10 μ.

Figure 13 shows a comparison of the above data with a curve calculated from Equation 10. The characteristic dimension, z, was chosen to give a best fit to the data in the least squares sense. The sonic limited curve is presented merely for reference. It can be seen that the temperature dependence of the heat pipe output agrees closely with that predicted by Equation 10.

It is interesting to speculate on the relation between screen geometry and the characteristic dimension in Equation 10, even though the available data are really insufficient for a firm conclusion. The screen geometry is specified by the screen opening, wire diameter, and wire spacing, only two of which are independent. Intuitively, the wave length of the most unstable disturbance on the liquid surface would seem to be related to the wire spacing, while the restoring force tending to restrain the liquid is related to the screen opening. If we take the observed characteristic dimension to be a weighted sum of the screen opening and wire spacing, we find relative weights of 1/3 and 2/3, respectively, for the 40 μ dimension of Fig. 13. Although use of this result well may be regarded as unjustified extrapolation from inadequate data, it also may be as good a result as can be obtained at present.

If Equation 10 is rewritten as

$$\frac{Q}{A}\sqrt{z} = h_{fg}\sqrt{g_c \rho_v \sigma} \ , \tag{11}$$

the right hand side becomes a function only of fluid properties. Thus, we may regard Equation 11 as defining the relative entrainment-limited power output of a given heat pipe for various fluids, since the left hand side of Equation 11 contains the only geometric parameters. Figure 14 is a plot of this entrainment parameter, defined by the right hand side of Equation 11, for cesium, potassium, sodium, and lithium.

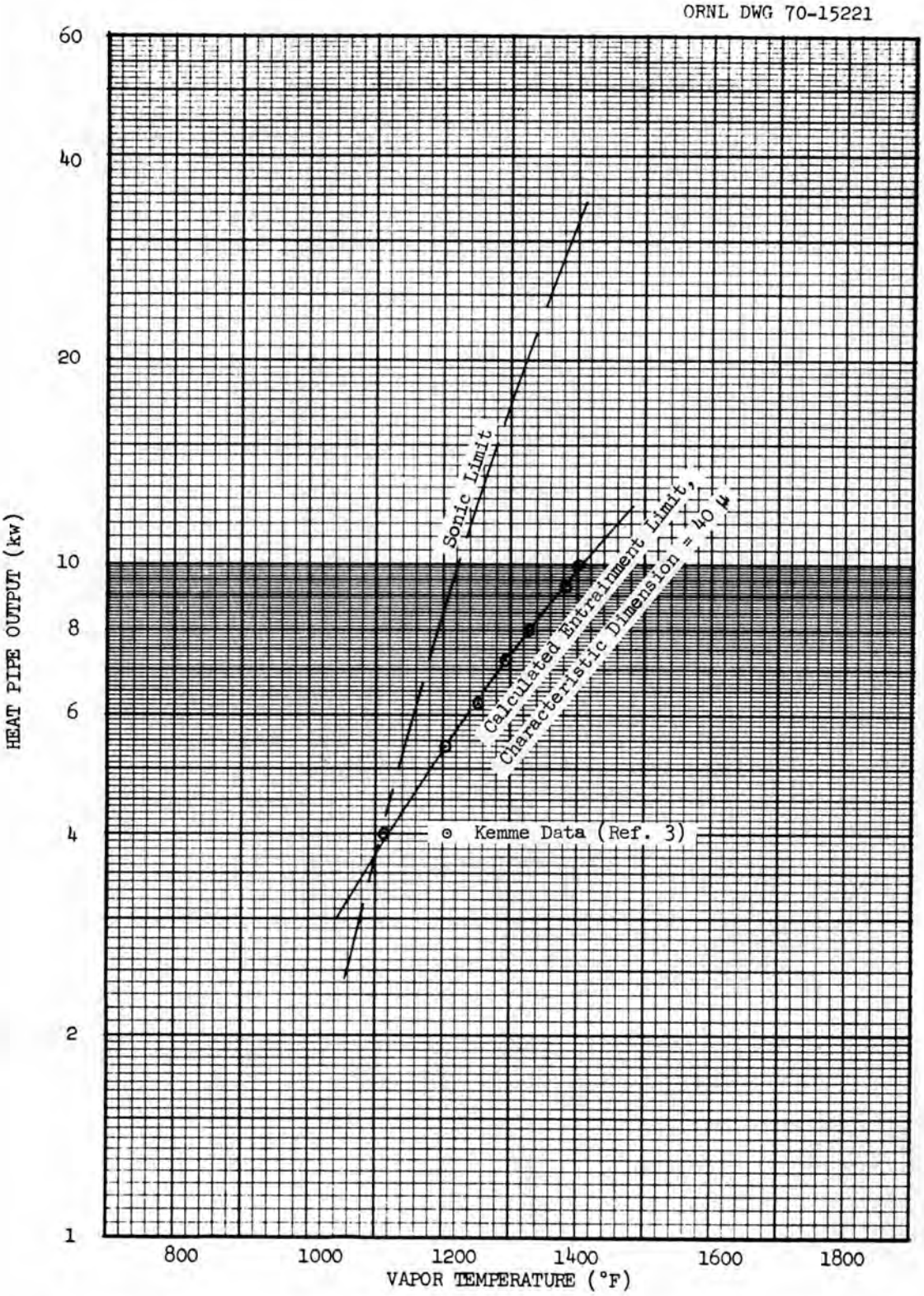

Fig. 13. Comparison of Calculated and Experimental Entrainment-Limited Output of a Sodium Heat Pipe. Characteristic dimension selected for best fit.

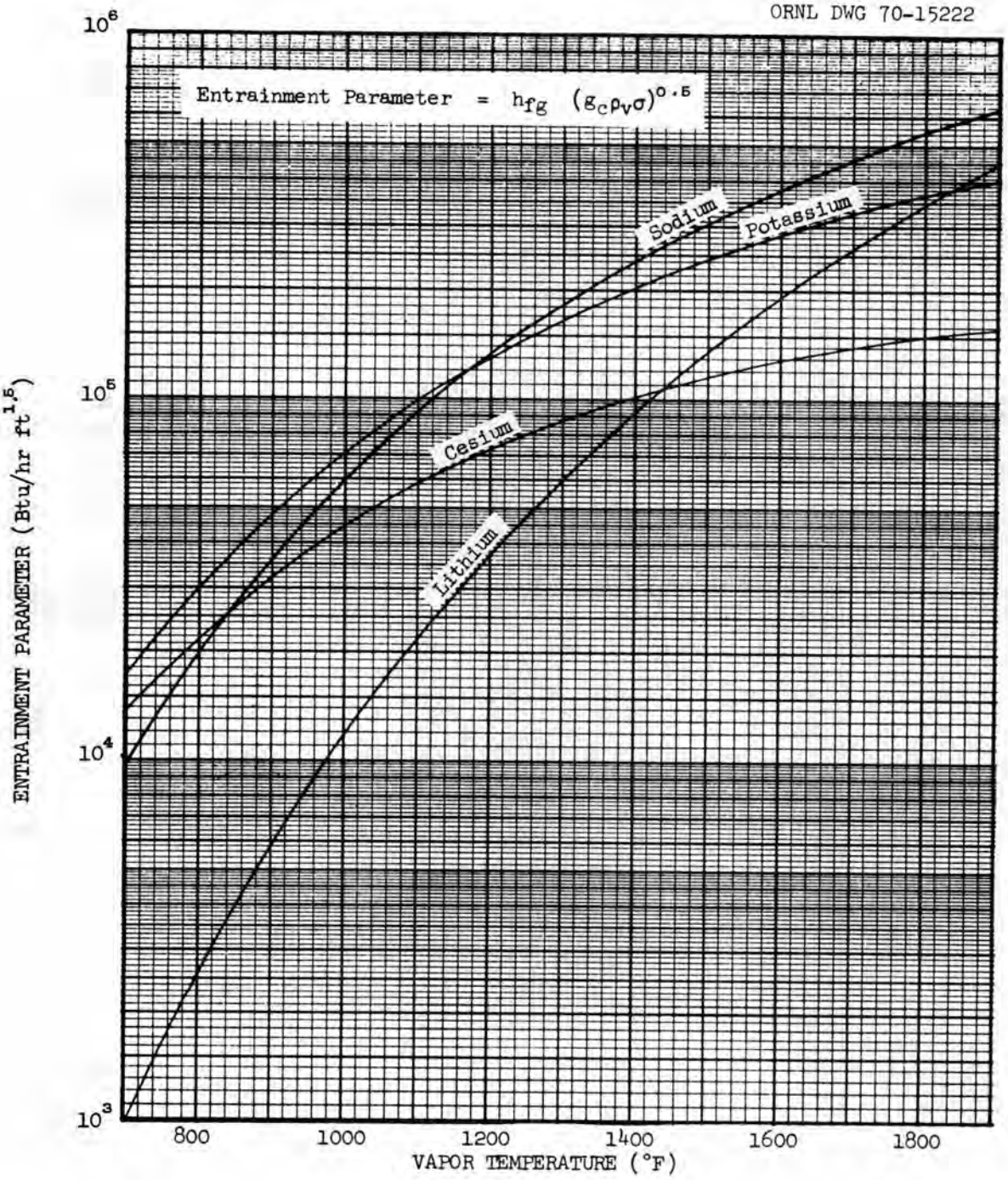

Fig. 14. Entrainment Parameter Based on Weber Number, Proportional to Heat Pipe Output at Entrainment Limit for Cesium, Potassium, Sodium, and Lithium.

Capillary Pumping

For steady-state operation of a heat pipe, the pressure rise available from capillary forces must just balance the pressure losses in the vapor and liquid circuits. That is, steady operation requires that

$$\begin{pmatrix}\text{capillary}\\ \text{pressure rise}\end{pmatrix} = \begin{pmatrix}\text{liquid-flow}\\ \text{pressure drop}\end{pmatrix} + \begin{pmatrix}\text{gravitational static}\\ \text{pressure difference}\end{pmatrix} + \begin{pmatrix}\text{vapor-flow}\\ \text{pressure drop}\end{pmatrix}$$

Cotter[2,21] has developed a theory for predicting the various terms in the above equation. The well-known relation between the pressure difference across a liquid-vapor interface and its principle radii of curvature is used to determine the capillary driving force. Darcy's law is applied in finding the liquid phase pressure drop, while the results from experiment and theoretical analyses are used in determining pressure drop in the vapor phase.

Capillary Pressure Rise

The expression for pressure difference across the curved liquid-vapor interface already has been given as Equation 1 in a previous section. For maximum performance, the principle radii of curvature of the interface should be equal, so that

$$\Delta P_c = \frac{2\sigma \cos \theta}{r_c}, \tag{12}$$

the added factor, $\cos \theta$, accounting for partial withdrawal of the meniscus into the capillary pore.

Liquid Pressure Drop

The liquid pressure gradient may be written, using Darcy's law, as

$$\frac{dP_l}{dZ} = \frac{g}{g_c} \rho_l \sin \phi - \frac{b\mu_l \dot{m}_l(Z)}{\pi e r_c^2 (r_w^2 - r_v^2)\, g_c \rho_l} \tag{13}$$

where, as defined by Cotter[2], b is a dimensionless constant characteristic of the capillary structure's geometry and e is the fraction of the wick volume that is occupied by liquid. Note that ϕ is defined in Fig. 1 such that a positive ϕ places the evaporator above the condenser.

With the reasonable assumption that mass flow, $\dot{m}(Z)$, varies linearly with Z in the evaporator and condenser and is a constant in the insulated sections, Equation 13 may be integrated to give

$$\Delta P_l = \frac{g}{g_c} \rho_l Z \sin \phi + \frac{b \mu_l (Z + Z_i)}{2\pi e r_c^2 (r_w^2 - r_v^2) g_c \rho_l} \frac{Q}{h_{fg}} \tag{14}$$

It should be noted that Equations 13 and 14 are one-dimensional in nature, whereas the actual liquid flow is obviously at least two-dimensional. However, as pointed out by Cotter[2], if the pipe is long and thin (that is, if $r_v Z$ is much greater than r_w^2) the radial pressure gradient in the liquid would be negligible in comparison with the axial gradient. One then may assume that both the pressure in the liquid and the flow velocity depend only on axial length.

Vapor Pressure Drop

A number of authors have noted the dynamic equivalence of channel flow with injection or suction through a porous wall to the vapor flow in the evaporator or condenser of a heat pipe. Yuan and Finkelstein[30] made a theoretical analysis of the flow in cylindrical pipes, while Knight and McInteer[31] analyzed the flow between plane parallel walls. Wageman and Guevara[32] performed both a theoretical analysis on a porous cylindrical tube and an experiment to verify the theoretical deductions. All of the analyses assumed incompressible laminar flow with uniform injection or suction along the porous wall.

For the purpose of distinguishing regimes of heat pipe operation, Cotter[2] defines a radial Reynolds number, R_r, based on the vapor density, the channel radius, the radial flow velocity at the channel wall, and the vapor viscosity. That is,

$$R_r = -\frac{\rho_v r_v v_r}{\mu_v} . \tag{15}$$

Note that, with this definition, R_r is positive for evaporation and negative for condensation.

High evaporation rates correspond to large radial Reynolds numbers. Since this is the regime of primary interest in heat pipe applications, only those portions of the analyses pertaining to large R_r will be discussed here.

For evaporation in cylindrical pipes, Wakeman and Guevara predicted theoretically and verified experimentally that the radial dependence of the axial velocity is not parabolic but, rather, is proportional to

$$\cos \frac{\pi}{2} \left(\frac{r}{r_v}\right)^2 .$$

The pressure decreases in the direction of flow and the flow properties may be calculated by a straightforward perturbation expansion in powers of the reciprocal Reynolds number.

Knight and McInteer have shown theoretically, for flow between plane parallel walls, that the evaporation and condensation cases are qualitatively different when the absolute value of R_r is large. With high condensation rates, the flow is of a boundary layer type wherein the axial velocity is substantially constant across most of the channel, the transition to zero velocity occurring in a thin layer adjacent to the wall. The pressure increases in the direction of fluid flow because of dynamic recovery in the decelerating fluid. Knight and McInteer have observed that, with the wall serving as a sink, the finite-viscosity perturbation solution does not converge uniformly to the zero-viscosity solution. The result is that self-consistent perturbation expansions cannot be made for this regime and only the limiting behavior, at present, can be described analytically.

In either case, for very large values of R_r, the pressure gradient can be shown to be given by

$$\frac{d\,P_v}{dZ} = -\frac{s\,\dot{m}_v}{4r_v^4\,\rho_v g_c}\,\frac{d\,\dot{m}_v}{dZ}\,, \tag{16}$$

where the difference in the two flows appears only in the value of the numerical coefficient, s. For evaporation, where the axial velocity has a radial cosine dependence, s = 1. For condensation, with a substantially constant axial velocity over most of the channel, $s = 4/\pi^2$. Integration of Equation 16, with the appropriate values of s, then yields, for the vapor pressure drop in the evaporator and condenser,

$$\Delta P_{vec} = \frac{1 - \frac{4}{\pi^2}}{8\,r_v^4\rho_v g_c}\left(\frac{Q}{h_{fg}}\right)^2 \tag{17}$$

It may be necessary, at times, to insert an insulated, or adiabatic, section (for which the net evaporation or condensation is essentially zero) between the evaporator and condenser. We then have, assuming Poiseuille flow,

$$\Delta P_{vi} = \frac{8\,\mu_v Z_i}{\pi\,r_v^4\rho_v g_c}\,\frac{Q}{h_{fg}}\,. \tag{18}$$

Overall Pressure Balance

As noted previously, for steady operation, the capillary pressure rise must just balance the pressure drops in the liquid and vapor flow circuits. Thus, consolidating results from Equations 12, 14, 17, and 18, we have for the overall pressure balance

$$\frac{2\sigma \cos \theta}{r_c} = \frac{1 - \frac{4}{\pi^2}}{8 r_v^4 \rho_v g_c} \left(\frac{Q}{h_{fg}}\right)^2 + \frac{8 \mu_v Z_i}{\pi r_v^4 \rho_v g_c} \frac{Q}{h_{fg}}$$

$$+ \frac{b \mu_l (Z+Z_i)}{2\pi e r_c^2 (r_w^2 - r_v^2) \rho_l g_c} \frac{Q}{h_{fg}} + \frac{g}{g_c} \rho_l Z \sin \phi \qquad (19)$$

With the specification of appropriate values for the constants b and e, Equation 19 may be used to calculate the capillary pumping limited output of a heat pipe. For example, in nonconnected parallel circular cylindrical pores[2], b = 8. For a concentric annular liquid passage, on the other hand, b = 24, e = 1, and r_c (on the right hand side, only, of Equation 19) must now be interpreted as the annulus width.

Comparison with Experiment

It should be noted that the several performance limitations discussed in previous sections are essentially independent of each other. For example, the expression for capillary limited power takes no account of the compressibility effect, and, in turn, the sonic flow limitation omits consideration of whether the developed capillary forces are, in fact, capable of sustaining such a flow. One would expect, then, that the actual output of a heat pipe under given operating conditions would be approximately the least value predicted by the several criteria above. That is, the observed performance curves should be the envelope, from the underside, of the several predicted performance curves. This point is illustrated in Fig. 15, where the calculated and experimental outputs of a heat pipe are compared, taking into account the sonic, entrainment, and capillary limits. Note that, at the lower temperatures, where compressibility effects are important, the performance of the heat pipe would have been grossly overestimated had it been based purely on the capillary pumping limitation. It can be seen that, except at the highest temperatures, the experimental curve corresponds fairly well to the envelope of the calculated curves.

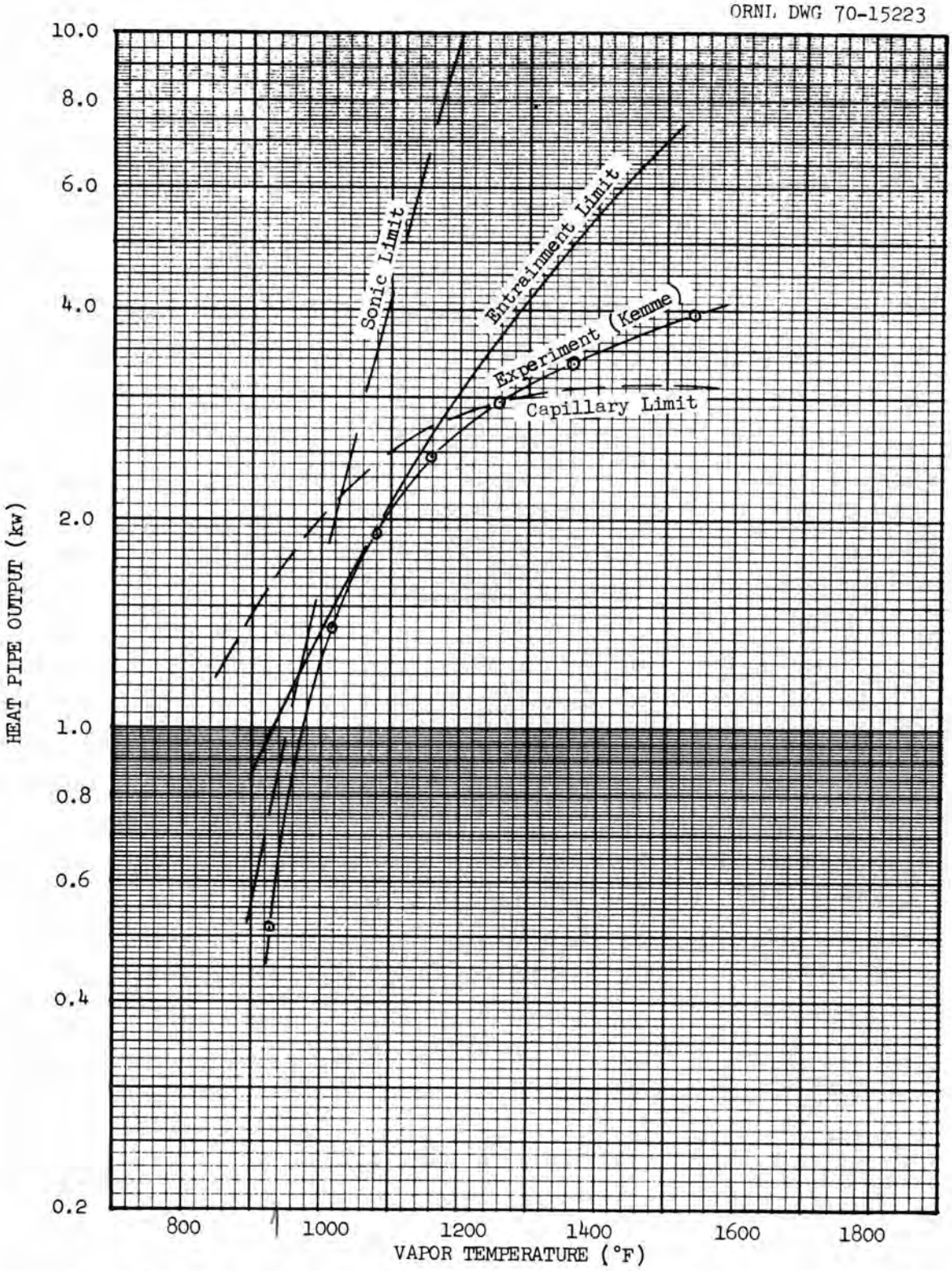

Fig. 15. Comparison of Calculated and Experimental Output of a Heat Pipe, Taking into Account the Sonic, Entrainment, and Capillary Limits.

The underestimate of capillary limited power at the higher temperatures may be connected with the overly conservative estimate of dynamic pressure recovery in the condenser. The assumptions leading to Equation 17 result in a predicted 40.5% pressure recovery in the condenser. However, it has been found that the amount of this recovery is difficult to predict for any particular set of operating conditions.

Flow Stability

An understanding of the theoretical stability of heat pipe flows, in the sense of transition from laminar to turbulent flow, appears to be lacking. Further, the available experimental evidence either appears to be conflicting or, at best, inconclusive.

Cotter[2] has suggested that, lacking better information one should use the laminar pressure drop formulas except for one case of practical interest. In a long insulated section interposed between evaporator and condenser of a heat pipe there will ordinarily be negligible mass addition or extraction. Then, for an axial Reynolds number (defined with the vapor radius) much in excess of 1000 and sufficient length of insulated section (say, a length greater than 50 vapor radii), one might use the empirical Blasius relationship for turbulent flow rather than the laminar relationship of Equation 18.

Bohdansky and Schins[33] investigated the laminar-turbulent transition in a 20 cm long, 0.8 cm diameter, adiabatic section of a heat pipe. The experimental pressure drop was determined by measuring inlet and exit temperatures and using the vapor pressure-temperature relationship for the fluid. Pressure drops were calculated for the same section for both laminar and turbulent flow. By comparing measured and calculated values, the authors estimated that the laminar-turbulent transition occurred at an axial Reynolds number of approximately 1500.

Wageman and Guevara[32] measured the radial variation of axial velocity in a cylindrical channel with gas injection through a porous wall. Excellent agreement was obtained between the experimental and theoretical profiles, although the theoretical distribution was derived for laminar flow,

whereas the experiments were done at axial Reynolds numbers up to 100,000, where one would expect turbulence to be well established. The authors note that compressibility effects were small at all flows.

OPTIMIZATION OF CAPILLARY LIMITED HEAT PIPES

Where heat pipe output is not limited by compressibility or entrainment effects, the question naturally arises as to whether an optimum geometry exists, such that the output computed from Eq. 19 is a maximum. Figure 16 shows that, for at least one capillary structure, this question is answered in the affirmative. It is the objective of this section to specify, somewhat more generally, the criteria for optimum proportions of several capillary structures.

Mesh and Channel Wicks

In both mesh and open channel wicks, a single dimension, the capillary radius, determines both the capillary pressure rise and the viscous contribution to the liquid pressure drop. The same thing is true of screen covered channels, if the size of the screen mesh is made proportional to the channel width. There then exist an optimum capillary radius and an optimum ratio between the vapor radius and the wall radius.

Optimum Capillary Radius

For convenience in manipulation, Eq. 19 may be written as

$$C_1 Q^2 + \frac{C_2 Z_e Q}{r_c^2} + C_3 Z_i Q + C_4 - \frac{C_5}{r_c} = 0 \quad , \tag{20}$$

where the coefficients C_1 thru C_5 are groupings of parameters that involve neither Q nor r_c. Z_e is the "equivalent length", $Z + Z_i$, of the heat pipe. If we then maximize Q with respect to r_c, the optimum capillary radius is found to be

ORNL DWG 70-15224

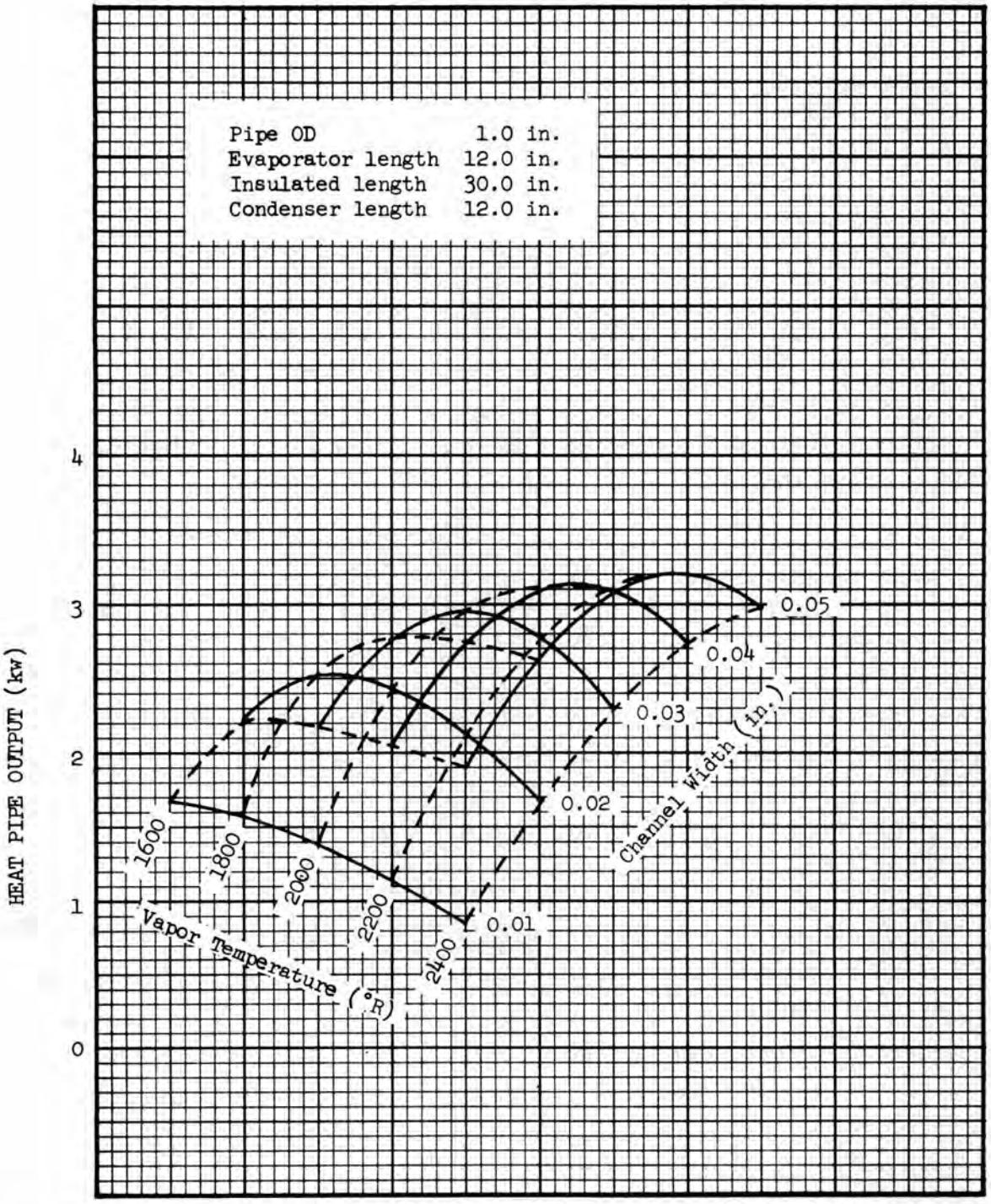

Fig. 16. Heat Pipe Output as a Function of Vapor Temperature and Capillary Width. Ratio of wall radius to vapor radius = 1.2. Fluid = Cesium.

$$r_c = \frac{2C_2 Z_e Q}{C_5} \quad . \tag{21}$$

Equation 21 may be rewritten to yield

$$\frac{C_2 Z_e Q}{r_c^2} = \frac{1}{2}\frac{C_5}{r_c} \quad , \tag{22}$$

that is, the maximizing condition is that the viscous portion of the liquid pressure drop should be exactly one half the capillary pressure rise, as noted by Cotter.[2]

If we eliminate Q between Eq. 20 and 21, Eq. 23 is obtained for the capillary radius, r_c.

$$\frac{C_1 C_5^2}{4C_2^2 Z_e^2} r_c^3 + \frac{C_3 C_5 Z_i}{2C_2 Z_e} r_c^2 + C_4 r_c - \frac{C_5}{2} = 0 \quad . \tag{23}$$

Similarly, eliminating r_c between Eq. 20 and 21 produces Eq. 24 for the maximum heat pipe output, Q.

$$C_1 C_2 Z Q^3 + C_2 C_3 Z_i Z_e Q^2 + C_2 C_4 Z Q - \frac{C_5^2}{4} = 0 \quad . \tag{24}$$

Equations 23 and 24 are, unfortunately, full-fledged cubic equations. While this presents no particular obstacle to a numerical solution, use of the known analytic solutions is likely to submerge any relationships in a welter of obscuring algebraic detail.

Let us consider, therefore, a more restricted problem, that of a heat pipe having no insulated section and operating either in a horizontal position or in a gravity free environment. Both the linear and the quadratic terms disappear from Eqs. 23 and 24 and we find that the optimum capillary radius is given by

$$r_c = \left[\frac{2C_2^3 Z^3}{C_1 C_5}\right]^{1/3} \quad , \tag{25}$$

and the corresponding maximum heat pipe output is given by

$$Q = \left[\frac{C_5^2}{4C_1 C_2 Z}\right]^{1/3} . \tag{26}$$

Optimum Radius Ratio

For a mesh wick, where the volume fraction occupied by liquid is a constant, the expression for maximum Q contains a factor, $r_v^4(r_w^2 - r_v^2)$, which attains its maximum for a radius ratio given by

$$\frac{r_v}{r_w} = \sqrt{\frac{2}{3}} . \tag{27}$$

The volume fraction, e, for longitudinal channels is a function of the number of channels and their shape. The expression for maximum Q now contains a factor, $r_v^5(r_w - r_v)$, which has a maximum at a radius ratio given by Eq. 28.

$$\frac{r_v}{r_w} = \frac{5}{6} . \tag{28}$$

Despite the rather large differences in detail of the above capillary structures, it should be noted that the optimum radius ratios differ only slightly, the second, in fact, being only 2% greater than the first.

Screened Annulus

As noted previously, for a concentric annular liquid passage, the quantity r_c on the right hand side of Eq. 19 must be interpreted as the annulus width. If, for simplicity, we make, a priori, the previous assumptions of no static head or insulated length, Eq. 19 may be written as

$$\frac{C_6 Q^2}{r_v^4} + \frac{C_7 Q}{(r_w + r_v)(r_w - r_v)^3} - C_8 = 0 \quad , \tag{29}$$

where the coefficients C_6 thru C_8 are now groupings of parameters not involving either Q or the vapor radius, r_v.

Unfortunately, if one attempts to determine an optimum vapor radius by maximizing Q in Eq. 29, the resulting equation in r_v proves to be a high-degree redundant polynomial equation for which no algebraic solution can be found. However, the existence of an optimum r_v is readily demonstrated as follows. For r_v sufficiently small, the first term in Eq. 29 is dominant and Q must decrease with r_v in order to maintain the equality. Thus, the slope of the curve is positive. On the other hand, for r_v sufficiently close to r_w, the second term in Eq. 29 is dominant. Here, Q must decrease as r_v increases in order, again, to maintain equality. The slope is, then, negative for r_v sufficiently close to r_w. Invoking merely the physically reasonable assumption that Q is a continuous function of r_v, it follows that an optimum value of r_v exists, for which Q is a maximum.

Figure 17 shows the results of some numerical experimentation performed with Eq. 29. Note that, in contrast with the results of the previous section, the optimum radius ratio is now a function of the vapor temperature. The optimum ratios are also somewhat higher than previously, those in the figure being approximately .93 to .94. Of the curves in Fig. 17, only that at the lowest temperature skirts the ragged edge of need to account for compressibility. Similar results would hold for both sodium and lithium with, however, the compressibility effects persisting to higher temperatures.

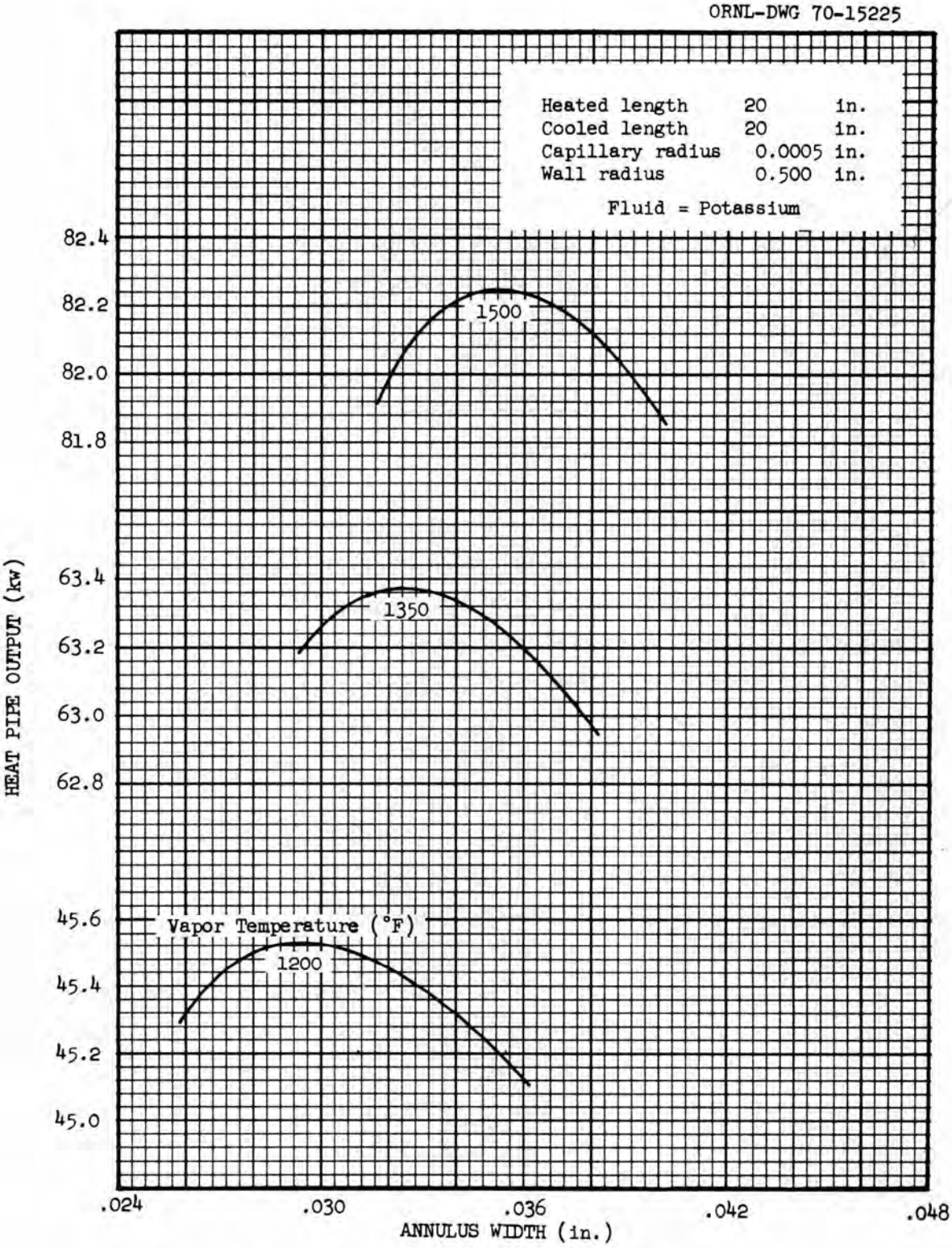

Fig. 17. Optimization of Annulus Width in a Screened Annulus Heat Pipe for Several Vapor Temperatures.

EFFECTS OF HEAT PIPE PARAMETERS

The parameters affecting heat pipe performance divide naturally into two categories, geometric and fluid. The objective of this section will be to examine, primarily by means of the theoretical relations previously obtained, the manner in which some of these parameters affect heat pipe output. As a general rule, the effect of a given parameter will depend to a considerable extent upon the auxiliary constraints placed on the remaining parameters and upon the heat pipe operating regime.

Geometric Effects

Diameter

Where the performance of a heat pipe is limited by sonic flow, the axial heat flux is a constant, as can be seen by reference to Eq. 6. That is, the output of the heat pipe is proportional to the square of the vapor diameter, independent of other geometric constraints. A similar conclusion obtains in the case of entrainment limitation, provided only that the characteristic dimension of Eq. 10 is held fixed.

Where capillary pumping is the performance limiter, a variety of results can be obtained depending upon the subsidiary geometric constraints imposed. Figure 18 shows the effect of vapor radius on heat pipe output for three such constraints.

Curve A illustrates the effect of varying the vapor radius while holding liquid flow area and the remaining linear dimensions of the heat pipe constant. The maximum in the curve appears because of the inter-relationship between vapor radius and annulus width. For sufficiently small vapor radii the annulus width is relatively large. As a result, the vapor pressure drop, which decreases with radius, dominates and the heat pipe output increases with radius. However, as the radius continues to increase, the progressively increasing liquid pressure drop becomes dominant and the heat pipe output begins to decrease.

If, now, we hold the annulus width and remaining linear dimensions other than the vapor radius constant, curve B is obtained. Here we obtain

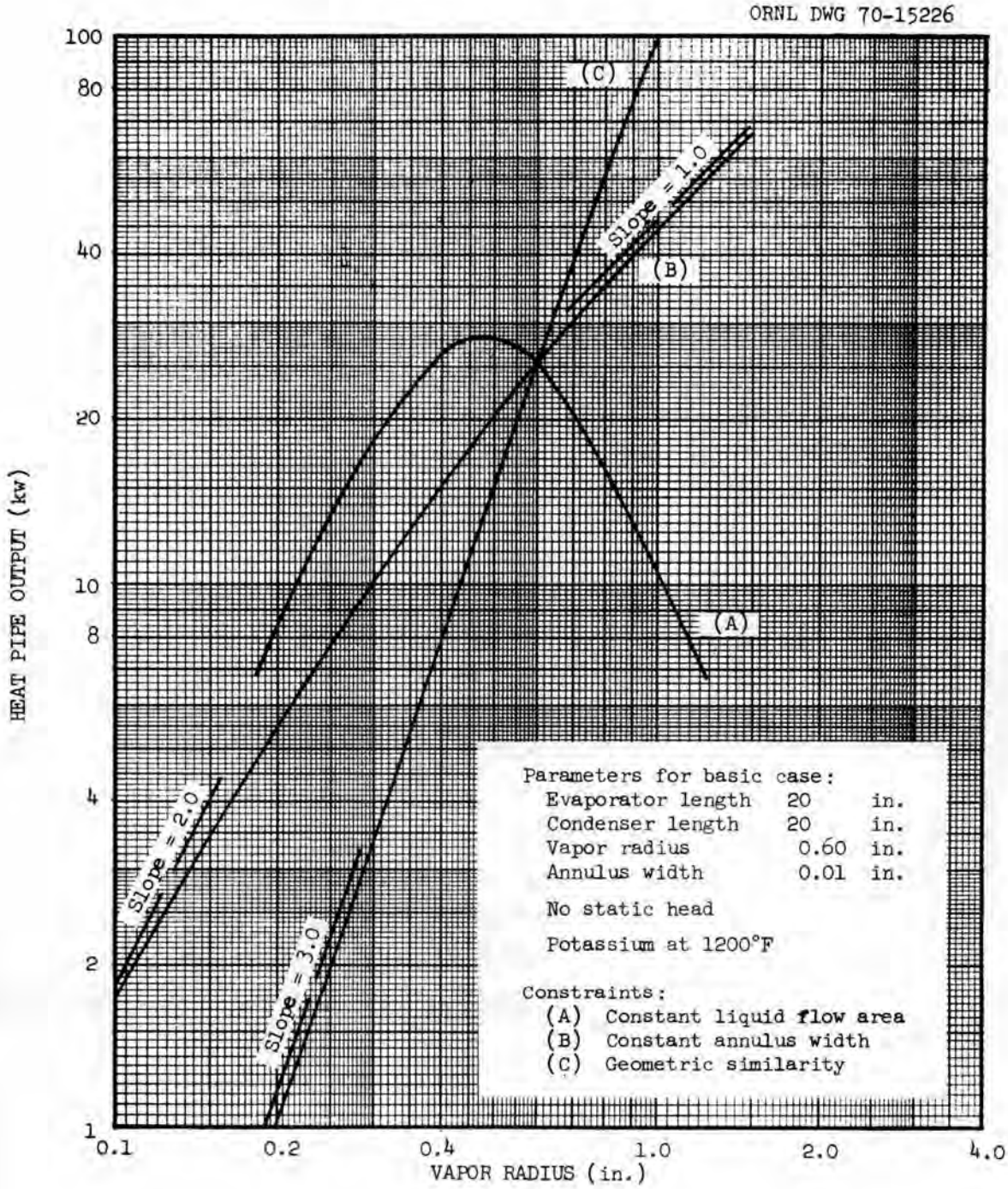

Fig. 18. Heat Pipe Output as a Function of Vapor Radius for Several Subsidiary Constraints.

an everywhere increasing output. For the small radii, where the momentum pressure drop is dominant, the curve asymptotically approaches a slope of 2 on a log-log plot, as in Fig. 18. For the larger radii, where the liquid pressure drop becomes important, the heat pipe output approaches a linear variation with radius, as indicated in Fig. 18 by the asympotic approach to a unit slope.

Finally, if complete geometric similarity is imposed, that is, the ratios of all the linear dimensions are held constant, one finds that, very nearly, the output is now proportional to the cube of the vapor radius. This means that the heat transport density is a constant as the vapor radius is varied. To put it differently, for a series of geometrically similar heat pipes, the output varies directly with the enclosed volume.

Length

As with diameter, the effect of length on heat pipe performance depends on the regime of operation. For sonic or entrainment limited operation, heat pipe output is independent of length. Where the operational limitation is capillary pumping, the variation of heat pipe output with length can be anything from independence to a reciprocal variation. This is shown in Fig. 19, where heat pipe output is plotted as a function of effective length for several annulus widths. Note that, for at least the two larger annulus widths, the heat pipe output approaches a constant for the shorter lengths, where the momentum pressure drop is most importance. It is clear from Fig. 19 that for the longer heat pipes output varies inversely with length. It will be observed that, in some cases, "long" can be very long indeed.

The lines indicated in Fig. 19 as having slopes of -1/3 are tangents drawn to their respective curves at the points where equality of pressure drop in the liquid and vapor phases was observed to occur. It is interesting to note that this same inverse variation of output with the cube root of heat pipe length is obtained from Eq. 26 for a heat pipe of quite different geometry but under the same restraint of pressure drop equality in the liquid and vapor phases.

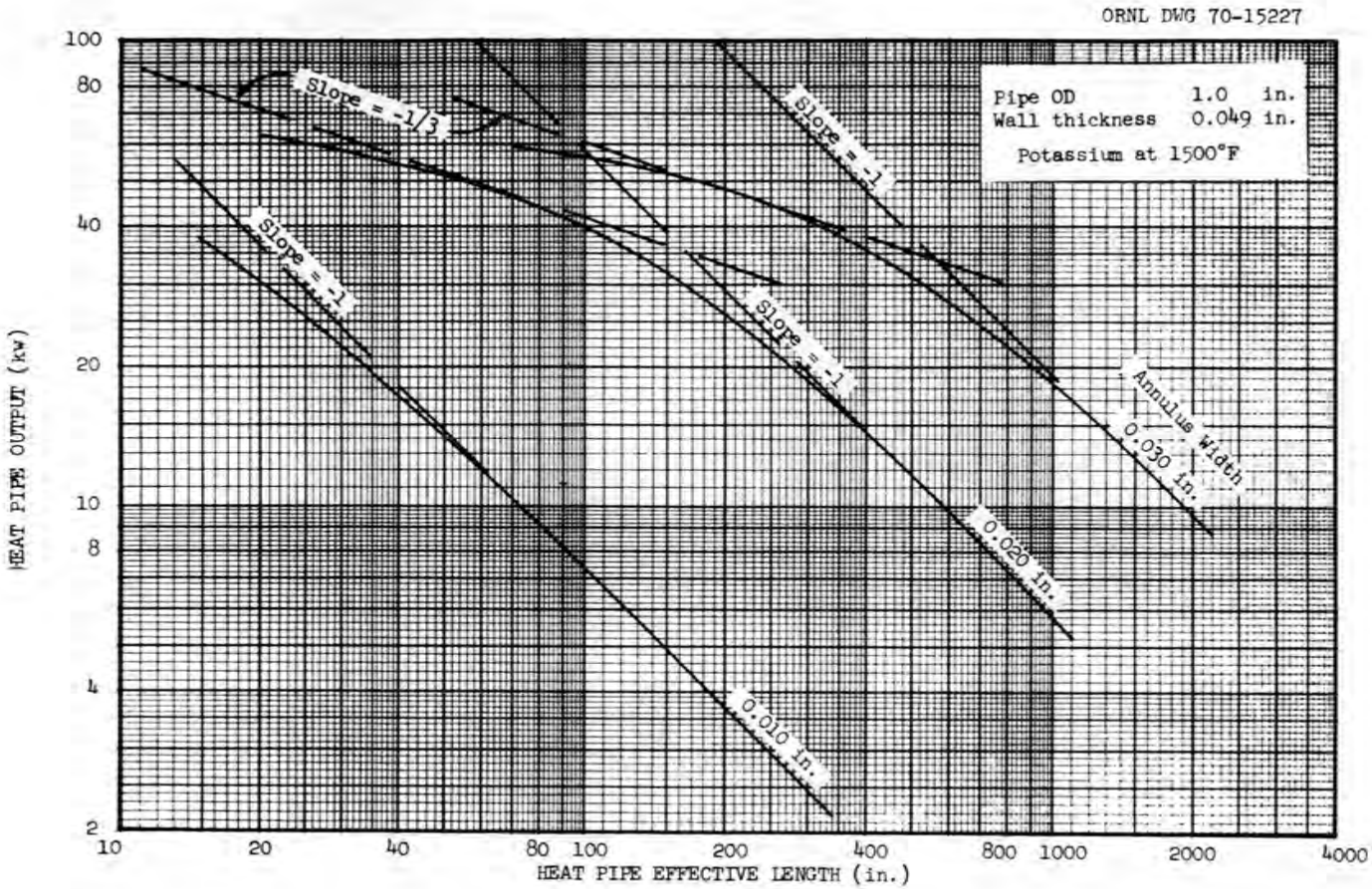

Fig. 19. Heat Pipe Output as a Function of Effective Length for Several Annulus Widths.

Annulus Eccentricity

Annulus eccentricity affects heat pipe performance by reducing the pressure drop in the annular space provided for liquid return. The magnitude of the reduction factor is readily estimated as follows. For the large ratios of the porous tube OD to the container ID commonly used, the width of the gap between the inner and outer tubes follows a cosine distribution around the perimeter very closely. For a constant mean diameter of the annulus, as is the case here, the pressure drop will vary inversely with the cube of the gap width. Then, integrating around the annulus, one finds that the pressure drop is reduced by a factor of 2.5 in going from a centered to a fully eccentric inner tube.

It is recognized that the equivalent diameter concept is not valid for laminar flow. However, the difference between annulus width and the theoretically correct linear dimension is negligible for the large radius to annulus thickness ratios employed in the screened annulus heat pipe, typically of the order of 50.

Attitude

Attitude of a heat pipe is meaningful only in the presence of a gravitational or other accelerational field, because of the liquid static head developed thereby. The component of this static head that effects heat pipe performance lies in the direction of the longitudinal axis of the heat pipe and is proportional to sin ϕ, where ϕ, as defined in Fig. 1, is the angle of inclination from the local horizontal.

Figure 20 shows the computed effect of orientation in a normal gravitational field on the performance of a liquid pressure drop limited heat pipe. As expected, the heat pipe output varies linearly with sin ϕ.

Note that, for this heat pipe, the static head in the vertical position, with the evaporator at the top, was very nearly enough to drive the output to zero. The heat pipe length at which the output does go to zero at any angle ϕ is readily determined from Eq. 19 by equating Q to zero and solving for Z, with the result that

$$Z_{max} = \frac{2\, g_c\, \sigma \cos \theta}{g\, \rho_l \sin \phi} \quad . \tag{30}$$

ORNL DWG 70-15228

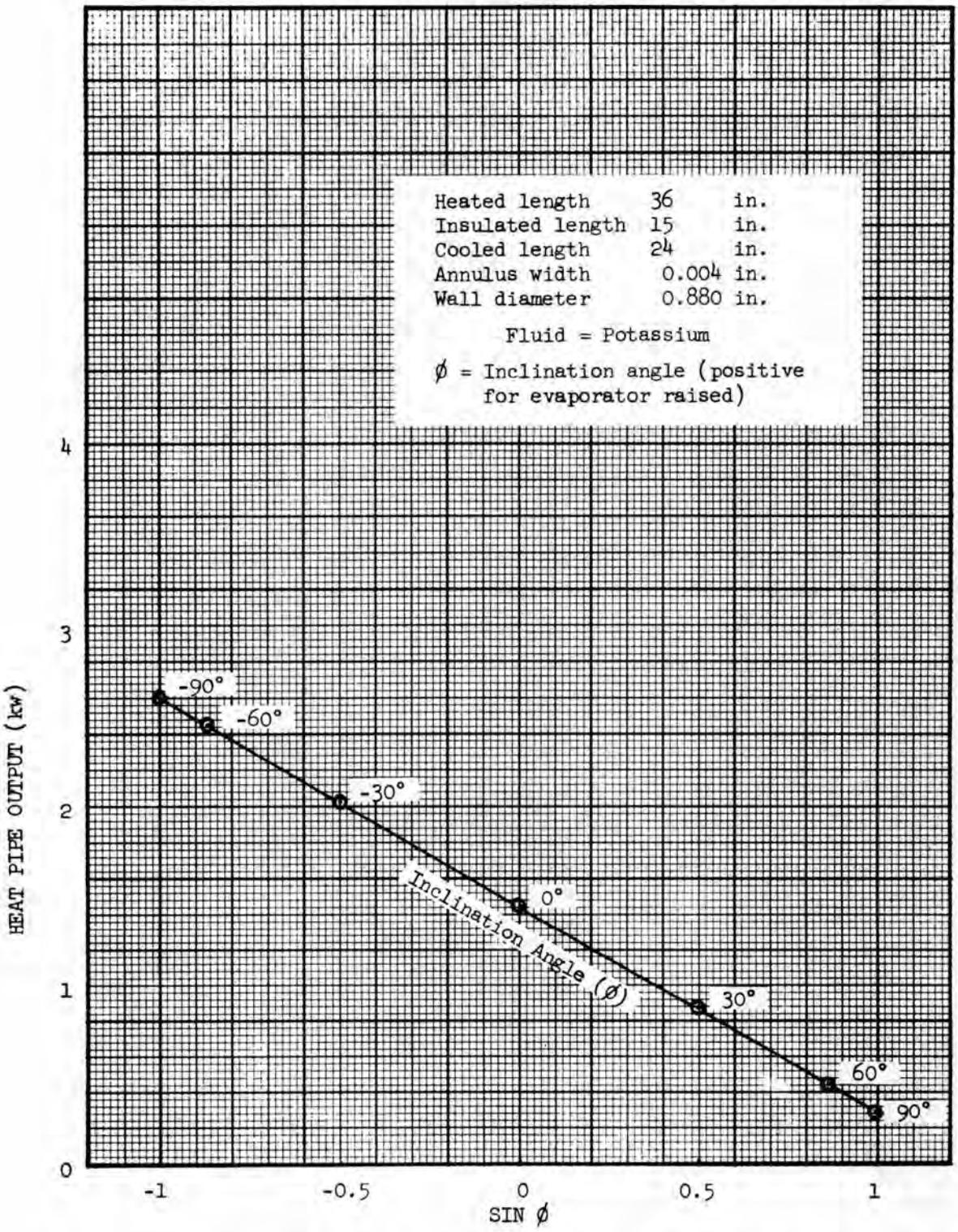

Fig. 20. Calculated Effect on Heat Pipe Output of Orientation in a 1-g Field.

Equation 30 is, of course, physically meaningful only for non-negative values of ϕ. For $\phi = 0$ (a horizontal heat pipe), Z_{max} is infinite.

Figure 21 is the experimental counterpart of Fig. 20 and shows the observed effect on heat pipe output of orientation in a 1-g field for several operating temperatures. The data were cross plotted from reference 34 and show the same essentially linear variation with sin ϕ as displayed in Fig. 20.

Fluid Effects

Some of the effects of varying the fluid and operating temperature have already been discussed in previous sections of this report. For example, characteristic sonic and entrainment parameters, containing only fluid properties, appear on the right hand side of Eqs. 6 and 11, respectively. Figures 10 and 14 are the corresponding graphical presentations of these parameters.

It is apparent from an examination of Eq. 19 that the effects of varying geometric and fluid parameters are entwined in a rather complex fashion. However, if one restricts attention to the optimized heat pipe discussed previously, it becomes possible to separate out the purely fluid characteristics. Equation 26 presents the output of a optimized heat pipe in terms of certain coefficients, whose values may be determined from a comparison of Eqs. 19 and 20. When this is done, the following grouping of fluid properties emerges.

$$h_{fg} \left[\frac{\rho_v \rho_l \sigma^2}{\mu_l}\right]^{1/3} .$$

This grouping, which is proportional to the maximized heat pipe output, is shown in Fig. 22 as a function of vapor temperature.

It is as important to keep firmly in mind what the figure does not show as what it does show. Figure 22 does not give the relative performance of the several fluids in a given heat pipe. Rather, the relative performance is that obtained for each fluid from a heat pipe proportioned to give maximum output at the given temperature. In other words, each point on

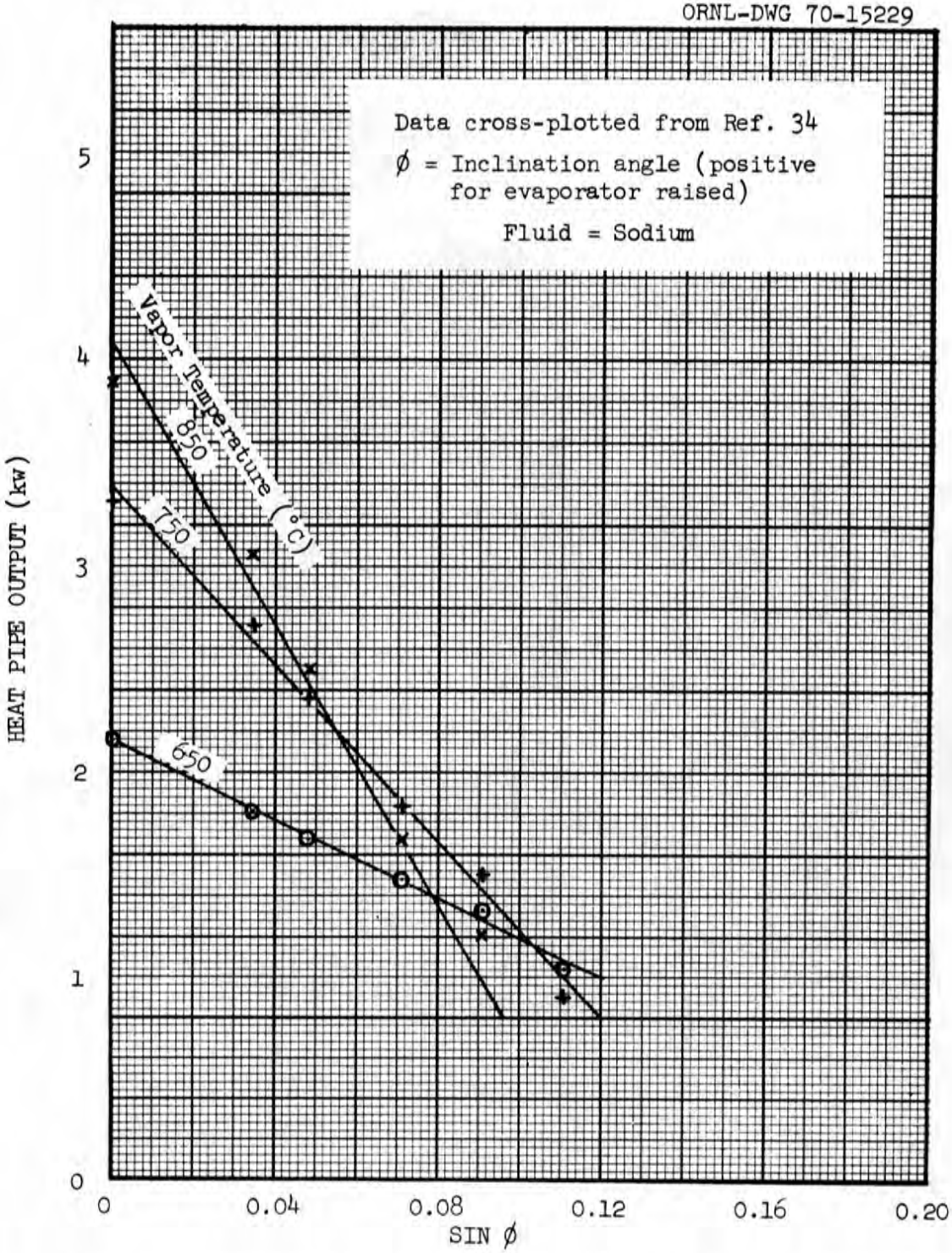

Fig. 21. Experimental Effect on Heat Pipe Output of Orientation in a 1-g Field.

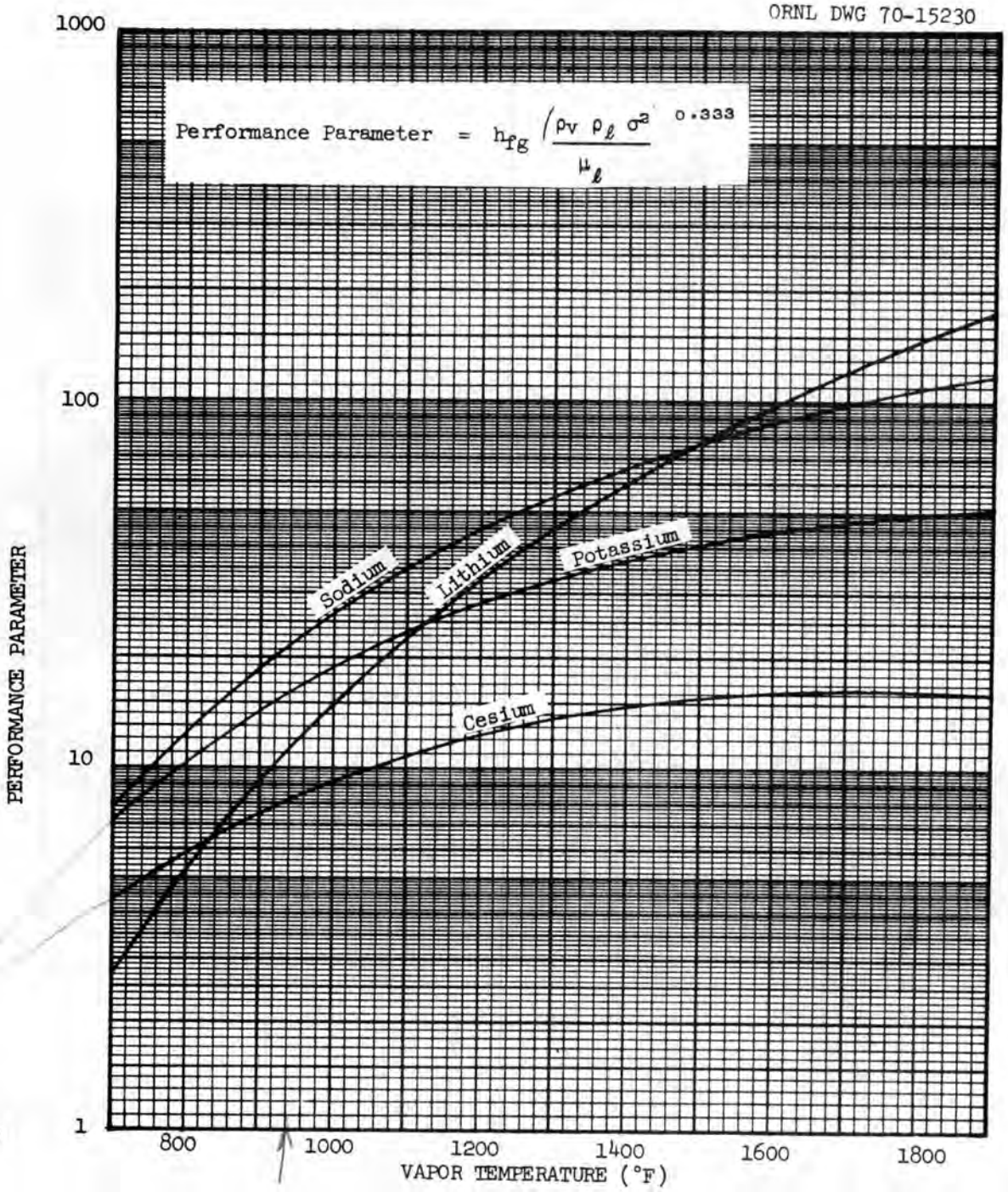

Fig. 22. Working Fluid Performance Parameter Based on Use in an Optimized Heat Pipe.

It is interesting to note that potassium exhibits performance superior to that of cesium over the entire temperature range plotted and is superior even to lithium up to roughly 1120°F. Sodium's performance is somewhat superior to potassium. However, if nearness to sonic flow is of importance, the substantially better performance shown in Fig. 10 for potassium could be an overriding consideration.

Neutron activation is a further consideration where, say, heat pipes are used for heat removal from a reactor core. Here, the substantially lesser activation of potassium, as compared to sodium, would be an important factor in its favor.

SUMMARY

The heat pipe is basically a two-phase flow device in which heat transport is effected by means of the latent heat of the fluid and fluid circulation is maintained by means of surface tension acting across a curved interface between the vapor and liquid. Because of its precise control of the location of the vapor-liquid interface, the heat pipe is well adapted to use in a gravity-free environment. Desirable properties for heat pipe working fluids include high surface tension, high latent heat of vaporization, high vapor density, low viscosity, and moderate vapor pressure.

The many, seemingly different, capillary structures used in heat pipes divide naturally into two basic types, the simple and the composite.

The simple type combines the differing functions of providing a liquid-return path and producing the required capillary driving force in a single structure. Because of their conflicting requirements, improvement in one of these functions is attained in the simple structure only at the expense of worsening the other. Thus, the simple capillary structure is inherently a relatively low performance type.

On the other hand, these two functions are largely separated in the composite structure. With the ability for essentially independent specification of the capillary force and liquid return path resistance, the composite wick is thus capable of relatively high performance.

However, the composite structures generally share the disadvantage of being more sensitive to emptying as a result of axial shock loading than

the simple structures, which tend to be self-healing. This disadvantage disappears, of course, for horizontal or gravity-free operation.

A multitude of heat pipe material and fluid combinations has been tested thus far and an extensive body of operating experience (substantially in excess of a quarter-million hours) accumulated. The heat pipe, being a two-phase, refluxing system, is subject to all the ills of such systems, including mass transfer and corrosion. However, the foregoing experience has shown that, with proper attention to materials compatibility, heat pipe assembly, and proper loading, the heat pipe is capable of long-term reliable operation without noticeable performance degradation.

As a two-phase flow system, with closely coupled liquid and vapor phases, the heat pipe is subject to certain performance limitations resulting from compressibility effects and vapor-liquid interactions. These limitations include sonic flow, liquid entrainment, and capillary pumping.

Sonic flow at the evaporator exit can be predicted by means of an analysis for the one-dimensional, steady, continuous flow of a semi perfect gas with injection. Despite the grossly simplified model, excellent agreement is obtained when a comparison is made between the analytic prediction and experimental data.

The entrainment limit is obtained from the theory of the dynamic instability of the interface between two fluids in relative motion. The condition for incipient stability involves a Weber number containing a characteristic dimension of the interface. Where a fine mesh screen is interposed between the two phases, the characteristic dimension is related to the screen dimensions. Very good agreement is obtained between the resulting prediction of the form of the entrainment limit dependence on temperature and that of the experimental data. While the available data are insufficient for a firm conclusion, a weighted mean of the screen opening and wire spacing is suggested as a possible predictor for the above characteristic dimension.

The prediction of pressure drop in determining the capillary pumping limit is based on an incompressible laminar flow analysis with uniform injection or suction. With injection or suction, corresponding to evaporation or condensation, the radial profiles of axial velocity differ radically from the parabolic profile obtained for laminar uniform flow. For evaporation,

the velocity profile may be determined from a perturbation expansion of the basic flow equations. This profile has been verified experimentally. On the other hand, self-consistent perturbation expansions cannot be made for condensing flow, so that only the limiting behavior can be described analytically. The result is a non-physical discontinuity in velocity profile at the juncture between evaporator and condenser, together with an underestimate of the pressure recovery in the condenser. Nevertheless, perhaps as a result of compensating errors, the capillary pumping limit is fairly well predicted. Where compressibility and entrainment are also of importance the resultant curve envelope represents the experimental results rather well.

In general, where heat pipe output is not limited by compressibility or entrainment, optimum geometric proportions, in the sense of maximized output, can be determined. In the simple capillary structure, both the capillary pressure rise and the viscous contribution to the liquid pressure drop are determined by a single dimension, the capillary radius. These pressure changes are affected in opposite directions and to a different degree by this single dimension. The result is that an optimum capillary radius and an optimum ratio between the vapor radius and the wall radius can be found. In the composite structure an optimum capillary radius no longer exists, the best value being the smallest that can be fabricated feasibly. An optimum ratio between the vapor and wall radii still exists, however, and is somewhat larger than that for the simple wick because of the relatively lower liquid resistance in the composite structure.

The parameters that effect heat pipe performance fall naturally into two categories, geometric and fluid. As a general rule, the effect of a given parameter will depend to a considerable extent upon the auxiliary constraints placed on the remaining parameters and on the heat pipe operating regime. For example, the effect of length on heat pipe performance varies from little or none, where the momentum pressure drop in the vapor is dominant, to a reciprocal relationship, where liquid pressure drop is dominant.

REFERENCES

1. G. M. Grover, T. P. Cotter, and G. F. Erickson, Structures of Very High Thermal Conductance, J. Appl. Phys., 35:1990–1991 (1964).

2. T. P. Cotter, Theory of Heat Pipes, LASL-LA-3246-MS, Los Alamos Scientific Laboratory, March 1965.

3. J. E. Kemme, High Performance Heat Pipes, pp. 355–358 in 1967 Thermionic Conversion Specialist Conference, USAEC Report CONF-671045-4, October 1967.

4. J. E. Kemme, Ultimate Heat Pipe Performance, IEEE Trans. on Electron Devices, ED-16(8):717-723 (1969)

5. J. E. Kemme, Heat Pipe Capability Experiments, LASL-LA-3585-MS, Los Alamos Scientific Laboratory, October 1966.

6. C. T. Ewing et al, High-Temperature Properties of Cesium, NRL-6246, U. S. Naval Research Laboratory, September 1965.

7. H. W. Hoffman and T. T. Robin, Jr., A Preliminary Collation of the Thermodynamic and Transport Properties of Cesium, USAEC Report ORNL-TM-1755, Oak Ridge National Laboratory, June 1967.

8. C. T. Ewing et al, High-Temperature Properties of Potassium, NRL-6233, U. S. Naval Research Laboratory, September 1965.

9. H. W. Hoffman and B. Cox, A Preliminary Collation of the Thermodynamic and Transport Properties of Potassium, USAEC Report ORNL-TM-2126, Oak Ridge National Laboratory, July 1968.

10. J. P. Stone et al, High-Temperature Properties of Sodium, NRL-6241, U.S. Naval Research Laboratory, September 1965.

11. P. Y. Achener et al, Thermophysical and Heat Transfer Properties of Alkali Metals, AGN-8195, Vol. I, Aerojet-General Corp., Nuclear Division, April 1968.

12. P. Y. Achener, Alkali Metals Evaluation Program, Quarterly Progress Report , 1 July–30 September 1966, AGN-8202, Aerojet-General Nucleonics, November 1966.

13. P. Y. Achener, Alkali Metals Evaluation Program, Quarterly Progress Report, 1 January–31 March 1967, AGN-8222, Aerojet-General Nucleonics, May 1967.

14. J. W. Cooke, The Experimental Determination of the Thermal Conductivity of Molten Lithium from 600 to 1550 Degrees Fahrenheit, Master's Thesis, University of Tennessee, December 1962.

15. W. D. Weatherford, Jr., et al, Properties of Inorganic Energy Conversion and Heat Transfer Fluids for Space Application, U.S. Air Force Report WADD TR 61-69, Aeronautical Systems Division, Wright-Patterson Air Force Base, 1961.

16. C. J. Meisl and A. Shapiro, Thermodynamic Properties of Alkali Metal Vapors and Mercury, Flight Propulsion Laboratory Department, General Electric Company, Report R60FPD358-A, November 1960.

17. K. Goldmann, R. Hankel, and R. P. Stein, An Equation for the Critical Mass Velocity of Homogeneous Vapor-Liquid Mixtures at Low Pressures, Trans. ASME, J. Appl. Mech., 86:380–382 (1964).

18. C. A. Busse et al, Performance Studies on Heat Pipes, International Conference on Thermionic Electrical Power Generation, London, Vol. 2 (1965).

19. G. Y. Eastman, The Heat Pipes — A Progress Report, Fourth International Energy Conversion Engineering Conference, Washington, D. C., pp. 873-878, September 1969.

20. T. K. Walters, Private Communication, Reactor Division Procurement, Oak Ridge National Laboratory.

21. T. P. Cotter et al, Status Report on Theory and Experiments on Heat Pipes at Los Alamos, International Conference on Thermionic Electrical Power Generation, London, Vol. 2 (1965).

22. K. Moritz, Ein Warmerohr neuer Bauart — das Gewinde-Arterien-Warmerohr (A New Design of Heat Pipe — The Thread Artery Heat Pipe), Chemie Ing. Techn., 41:37–40 (1969).

23. C. A. Busse, Heat Pipe Thermionic Converter Research in Europe, Fourth Intersociety Energy Conversion Engineering Conference, Washington, D. C., pp. 861–872, September 1969.

24. J. H. DeVan and D. H. Jansen, Examination of RCA Heat Pipes, USAEC Report ORNL-TM- , Oak Ridge National Laboratory, (to be published).

25. J. E. Deverall and J. E. Kemme, High Thermal Conductance Devices Utilizing the Boiling of Lithium or Silver, LASL-LA-3211, Los Alamos Scientific Laboratory, April 1965.

26. J. E. Deverall, Mercury as a Heat Pipe Fluid, LASL-LA-4300-MS, Los Alamos Scientific Laboratory, January 1970.

27. A. H. Shapiro, The Dynamics and Thermodynamics of Compressible Fluid Flow, Vol. I, pp. 219–260, The Ronald Press, New York, 1953.

28. T. P. Cotter, Heat Pipe Startup Dynamics, pp. 344–348 in 1967 Thermionic Conversion Specialist Conference, USAEC Report CONF-671045-4, October 1967.

29. H. Lamb, Hydrodynamics, Art. 268, Sixth Edition, Dover Publications, New York, 1945.

30. S. W. Yuan and A. B. Finkelstein, Laminar Pipe Flow with Injection and Suction Through a Porous Wall, Trans. ASME, 78:719–724 (1956).

31. B. K. Knight, Jr., and B. B. McInteer, Laminar Incompressible Flow in Channels with Porous Walls, LA-DC-5309, Los Alamos Scientific Laboratory.

32. W. E. Wageman and F. A. Guevara, Fluid Flow through a Porous Channel, Phys. Fluids, 3:878–881 (1960).

33. J. Bohdansky and H. E. J. Schins, Heat Transfer of a Heat Pipe Operating at Emitter Temperatures, International Conference on Thermionic Electrical Power Generation, London, Vol. 2 (1965).

34. J. Bohdansky, H. Strub, and E. van Andel, Heat Transfer and Energy Conversion in a Thermionic Diode, International Conference on Thermionic Electrical Power Generation, London, Vol. 2 (1965).

APPENDICES

Appendix A

FORTRAN SUBROUTINES FOR COMPUTING THE THERMODYNAMIC AND TRANSPORT PROPERTIES OF CESIUM, POTASSIUM, SODIUM, AND LITHIUM

This Appendix contains a computer-prepared printout of the FORTRAN subroutines written for the Call-A-Computer (CAC) time-sharing remote terminal computing system in use in this Division. These subroutines were used to calculate fluid properties for Figs. 2-7, 10-20, and 22. The calling sequence is:

```
CALL FLPRØP(N,T,P,DENL,VISL,CØNL,CPL,SIG,DENV,VISV,HFG,GS)
```

where input

N = fluid number (see subroutine printout),

T = vapor temperature, °R,

and output

P = vapor pressure, psia,

DENL = liquid density,

VISL = liquid viscosity,

CØNL = liquid conductivity, Btu/hr·ft·°R,

CPL = liquid specific heat,

SIG = liquid surface tension,

DENV = vapor density,

VISV = vapor viscosity,

HFG = latent heat of vaporization,

GS = sonic mass flow rate per unit area, $lb_m/hr \cdot ft^2$.

Units are as given in Appendix B, except where specified above.

Although FORTRAN has been purported to be a machine-independent programming language, the sad reality of computing life is that almost every version of FORTRAN differs from every other in some respect, with the CAC version being no exception. Note, for example, that the statements are not written in a standard card format, that is, comments are not introduced by a "C" in column 1, statements do not have to start in column 7, etc. For this reason, the following comments on features possibly peculiar to

the CAC FORTRAN are offered in order to minimize conversion problems for potential users:

1. Line numbers. These are used purely for system bookkeeping and should be deleted. They are not statement numbers.

2. Comments. Comments may be inserted in several ways in CAC FORTRAN. The way used here is to enter a nonblank character (in this case, an asterisk) immediately after the line number. Lines 100, 110, 120, and 170 are comment lines.

3. Continuation: A statement is continued from one line to the next by inserting a plus sign as the first nonblank character of each continuation line. Thus, line 140 continues the statement begun in line 130. In "standard" card format FORTRAN, lines such as 460 and 680, where there is no space between the statement number and the statement, are likely to generate syntactical error messages because of confusion with continuation lines. Insertion of at least one space should cure the problem.

4. Blank lines. Blank lines, useful for visual separation of program sections, may be inserted by typing any non-numeric character immediately after the line number and then terminating the line. For example, line 180 uses a single blank (space) whereas line 120 (which is also a comment line, by definition) uses an asterisk.

5. Multiple statements per line. As many statements as will fit may be put on a single line, if desired. The semicolon is used as a separator between statements. Line 150, for example, contains a declaration statement and two arithmetic statements.

6. Arithmetic IF. The CAC arithmetic IF allows truncation of the statement number list under special circumstances. For example, if the expression in line 430 is positive, control passes to line 440 (the next statement) by default, since the transfer on a positive value was not specified. If only one statement number had been given, control would have passed to line 440 on both zero and positive values of the expression.

FLPRØP

```
100*            M. LAVERNE   9102   3-5702
110*            26 MAY 1970
120*
130   SUBRØUTINE FLPRØP
140  +(NFLUID,TR,PSIA,RHØL,MUL,KL,CPL,SIG,RHØV,MUV,HFG,GS)
150   REAL KL,MUL,MUV; TLØG = LØG(TR); TF = TR-459.69
160   GØ TØ (4,5,6,7) NFLUID
170*          NFLUID: 1=K; 2=LI; 3=NA; 4=CS
180
190 4 PSIA = EXP(16.79685-0.53299*TLØG-18717.1/TR)
200   RHØL = 52.768+((4.98E-11*TF-5.255E-7)*TF-7.4975E-3)*TF
210   IF (TR-1157.922) 1,1,2
220 1 MUL = EXP(1189.98/TR-1.62862); GØ TØ 3
230 2 MUL = EXP(1698.16/TR-2.06749)
240 3 KL = 28.831-7.1311E-3*TR+4111.0/TR
250   SIG = (911.37-0.24591*TR)*1.0E-5; MUV = 1.573E-3*SQRT(TR)
260   A = 9.31436E-2*PSIA/TR; B = -EXP(TLØG+11261./TR-8.9310)
270   C =  EXP(14704./TR+1.3523); D = -EXP(18107./TR+3.3606)
280   CALL VIRIAL(RHØV,39.1,A,B,C,D,0.)
290   HFG = 0.18504*PSIA*(18717.1/TR-0.53299)*(1.0/RHØV-1.0/RHØL)
300   CPL = (.2317E-7*TR-.6483E-4)*TR+.2271; GØ TØ 11
310
320 5 PSIA = EXP(1.9390*TLØG-26936.5/TR-3.51184)
330   RHØL = 15.933+0.2469*SQRT(5711.69-TR)-1.4342E-3*TR
340   MUL = EXP(11.88996-646.529/TR-1.61506*TLØG)
350   KL = 15.209+0.0099*TR; MUV = 2.65E-4*TR↑0.65
360   SIG = 3.1637E-2 - 5.5390E-6*TR+4.0651E3*EXP(-TR/55.0)
370   HFG = 10910.16*(1.0-TR/5711.61)↑0.3725
380   VV = 1.0/RHØL+HFG/(0.18504*PSIA*(26936.5/TR+1.939))
390   RHØV = 1./VV; CPL = 1.017875-1.6E-5*TF; GØ TØ 11
400
410 6 PSIA = EXP(18.432-22982./TR-.61344*TLØG)
420   RHØL = ((6.035E-11*TF-2.872E-7)*TF-7.9504E-3)*TF+59.566
430   IF(TF-932.) 9,9
440   MUL = .0437*RHØL↑.33333*EXP(30.0*RHØL/TR); GØ TØ 10
450 9 MUL = .0635*RHØL↑.33333*EXP(20.1*RHØL/TR)
460 10KL = 53.5824-.01574*TF
470   SIG = .0139-3.807E-6*TF; MUV = .03+8.57E-6*TR
480   A = 9.31436E-2*PSIA/TR; B = -EXP(TLØG+15555./TR-10.021)
490   C = EXP(24958./TR-1.4131); D = -EXP(31175./TR-.2084)
500   CALL VIRIAL(RHØV,22.997,A,B,C,D,0.)
510   HFG = .18504*PSIA*(22982./TR-.61344)*(1./RHØV-1./RHØL)
520   CPL = (4.057E-8*TF-9.415E-5)*TF+.3525; GØ TØ 11
530
560 7 PSIA = EXP(16.21075-0.53290*TLØG-16211.8/TR)
570   RHØL = 124.181-(1.6855E-6*TR+1.597E-2)*TR
580   MUL = EXP(3.2574-0.59911*TLØG+431.097/TR)
590   KL = 16.220-3.995E-3*TR
600   SIG = 6.1062E-3-1.9376E-6*TR; MUV = 1.118E-3*TR↑.5241
610   A = 9.31436E-2*PSIA/TR; B = -EXP(TLØG+9210.34/TR-8.33536)
```

FLPRØP CØNTINUED

```
620    C = EXP((24.9255E6/TR-12.2762E3)/TR+7.72540)
630    D = -EXP(9.6377+2026.3/TR)
640    CALL VIRIAL(RHØV,132.91,A,B,C,D,6.E5)
650    HFG = 0.18501*PSIA*(16211.8/TR-0.53290)*(1.0/RHØV-1.0/RHØL)
660    CPL = 0.05683; GØ TØ 11
670
680 11ALPHA = PSIA/(5.40458*RHØV*HFG)
690    BETA = CPL*TR*ALPHA/HFG
700    GS = SQRT((6.00444E10*PSIA*RHØV)/(1.-2.*ALPHA+BETA))
710    RETURN
720    SUBRØUTINE VIRIAL(RHØ,WM,A,B,C,D,E); VM = 1./A
730    DØ 1 I = 1,20; DER = 0.; F = A
740    DER = F+VM*DER; F = -1.+VM*F; DER = F+VM*DER
750    F = -B+VM*F; DER = F+VM*DER; F = -C+VM*F
760    DER = F+VM*DER; F = -D+VM*F; DER = F+VM*DER
770    F = -E+VM*F; DVM = F/DER; VM = VM-DVM
780    IF (.001-ABS(DVM)) 1,2,2
790 1 CØNTINUE
800 2 RHØ = WM/VM; RETURN; END
```

LENGTH
ABØUT 3400 CHARS.

Appendix B

NOMENCLATURE

This Appendix contains a listing of the symbols used in this report, together with a brief description and the units for each. Although any consistent set of units could be used, the particular set given here was picked to conform to the usage in Subroutine FLPRØP of Appendix A.

Symbol	Meaning	Units
A	Axial vapor-flow area	ft^2
b	Wick pressure-drop parameter	
C_1 to C_8	Coefficients defined by Eqs. 20–26 and 29	
e	Liquid fraction of wick volume	
g	Acceleration of gravity	ft/hr^2
g_c	Conversion constant	$4.170 \cdot 10^8$ lb_f ft/lb_m hr^2
h_{fg}	Latent heat of vaporization	Btu/lb_m
k	Ratio of specific heats	
$\dot{m}$	Mass flow rate	lb_m/hr
M	Mach number	
P	Pressure	lb_f/ft^2
ΔP	Pressure difference	lb_f/ft^2
Q	Heat transport rate	Btu/hr
r	Radius	ft
R	Reynolds number based on radius	
s	Coefficient defined for Eq. 16: $s = 1$ for evaporation; $s = 4/\pi^2$ for condensation	
V	Flow velocity	ft/hr
We	Weber number	
z	Characteristic entrainment dimension	ft
Z	Heat pipe axial length	ft
θ	Angle between liquid surface at contact with pore surface and perpendicular to mean vapor-liquid interface	deg
μ	Viscosity	$lb_m/hr \cdot ft$

Symbol	Meaning	Units
ρ	Specific weight	lb_m/ft^3
σ	Surface tension	lb_f/ft
ϕ	Angle from local horizontal	deg

Subscripts:

c	Channel or condenser, depending on context
e	Evaporator or equivalent, depending on context
i	Insulated section
l	Liquid
r	Radial
s	Sonic
v	Vapor
w	Wall

Internal Distribution

1. S. E. Beall
2. T. A. Butler
3. W. B. Cottrell
4. W. C. Cox
5. F. L. Culler
6. R. G. Donnelly
7–16. A. P. Fraas
17. J. H. Frye, Jr.
18. J. H. Gillette
19. A. G. Grindell
20. K. W. Haff
21. H. W. Hoffman
22. R. S. Holcomb
23. P. R. Kasten
24. M. E. Lackey
25. E. Lamb
26-35. M. E. LaVerne
36. D. B. Lloyd
37. M. I. Lundin
38. R. N. Lyon
39. R. E. MacPherson
40. H. C. McCurdy
41. A. J. Miller
42. A. M. Perry
43. R. A. Robinson
44. M. W. Rosenthal
45. A. F. Rupp
46. G. Samuels
47. A. W. Savolainen
48. A. C. Schaffhauser
49. M. J. Skinner
50. A. M. Smith
51. I. Spiewak
52. D. A. Sundberg
53. D. B. Trauger
54. J. J. Tudor
55. A. M. Weinberg
56. G. D. Whitman
57. J. V. Wilson
58. H. C. Young
59. Biology Library
60-61. Central Research Library
62. Y-12 Technical Library – Document Reference Section
63–92. Laboratory Records Department
93. Laboratory Records Department (RC)

External Distribution

94. E. P. Baranowski, Division of Production AEC, Washington, D. C. 20545
95. D. R. Bartz, Jet Propulsion Lab., NASA, 4800 Oak Grove Drive, Pasadena, California 91103
96. H. Bibb, Naval Facilities Engineering Command, Washington, D. C. 20390
97. D. Bogart, NASA, Lewis Research Center, Cleveland, Ohio 44135
98. R. Breitwieser, NASA, Lewis Research Center, Cleveland, Ohio 44135
99. Les Chadbourne, AiRearch Manufacturing Company, 402 S. 36th Street, Phoenix, Arizona 85034
100. D. F. Cope, RDT Site Office, ORNL
101. W. M. Crim, Jr., Research and Technology Department, Building 322, Ft. Belvoir, Virginia 22060
102. R. R. Dahlen, Advanced Engineering, 3-M Company, Building 551, 2501 Walnut Street, Roseville, Minnesota 55113
103. R. V. Degner, Rocketdyne, 6633 Canoga Avenue, Canoga Park, California 91303
104. R. N. Endebrock, Isotopic Auxiliary Power Branch, AEC, Washington, D. C. 20545

105. R. E. English, NASA, Lewis Research Center, Cleveland, Ohio 44135
106. E. E. Fowler, Division of Isotopes Development, AEC, Washington, D. C. 20545
107. N. C. Gibbon, Cryogenic Products Department, Linde Division, P. O. Box 44, Tonawanda, New York 14150
108. J. C. Graf, General Electric, Valley Forge, Pennsylvania 19481
109. G. Grover, Los Alamos Scientific Laboratory, P. O. Box 1663, Los Alamos, New Mexico 87544
110-114. W. D. Holloman, Division of Reactor Development and Technology, AEC, Washington, D. C. 20545
115. C. E. Johnson, Los Alamos Scientific Laboratory, P. O. Box 1663, Los Alamos, New Mexico 87544
116. S. Kauffman, Lewis Research Center, Cleveland, Ohio 44135
117. J. E. Kemme, Los Alamos Scientific Laboratory, P. O. Box 1663, Los Alamos, New Mexico 87544
118. M. Klein, Division of Reactor Development and Technology, AEC, Washington, D. C. 20545
119. E. Lantz, Lewis Research Center, Cleveland, Ohio 44135
120. G. S. Leighton, Sundstand Aviation, 1100 Connecticut Avenue, N.W., Washington, D. C. 20036
121. J. J. Lynch, NASA Headquarters, Washington, D. C. 20546
122. S. V. Manson, NASA Headquarters, Washington, D. C. 20546
123. R. F. Mather, NASA, Lewis Research Center, Cleveland, Ohio 44135
124. C. McCallum, Los Alamos Scientific Laboratory, P. O. Box 1663, Los Alamos, New Mexico 87544
125. B. T. McCauley, Aerojet-General Corp., Azusa, California 91702
126. R. E. Niggeman, Sundstand Aviation, 4747 Harrison Avenue, Rockford, Illinois 61101
127-131. Nuclear Engineering Division, Naval Facilities Engineering Command, Washington, D. C. 20390
132. J. Pidkowicz, RDT Site Office, ORNL
133. W. D. Pouchot, Westinghouse Astronuclear Laboratory, P. O. Box 10864, Pittsburgh, Pennsylvania 15236
134. D. F. Rife, Westinghouse, Lima, Ohio 45801
135. D. R. Roberts, Westinghouse Astronuclear Laboratory, P. O. Box 10864, Pittsburg, Pennsylvania 15236
136. F. E. Rom, NASA, Lewis Research Center, Cleveland, Ohio 44135
137. C. R. Ross, Savannah River Laboratory, Aiken, S. C. 29801
138. George Shepherd, Fairchild Technology Corp., One Goddard Drive, Rockaway, New Jersey 07866
139. G. W. Sherman, Aeronautical Space Power Division, Air Force Aeronautical Propulsion Laboratory, Wright-Patterson Air Force Base, Ohio 45433
140. H. O. Slone, NASA, Lewis Research Center, Cleveland, Ohio 44135
141. Anthony Stathoplos, Nuclear Technology Corporation, 116 Main Street, White Plains, New York 10600
142. B. Sternlicht, Mechanical Technology, Inc., 968 Albany-Shaker Road, Latham, New York 12110
143. D. Stewart, Battelle Northwest Laboratory, Richland, Washington 99352

144. P. Swenson, Jr., Swenson Research Inc., 5135 Richmond Road, Bedford Heights, Ohio 44146
145. J. E. Taylor, Thompson-Ramo-Wooldridge, 23555 Euclid Avenue, Cleveland, Ohio 44117
146. W. B. Taylor, Technical Director, U. S. Army Mobility Equipment Research and Development Center, Ft. Belvoir, Virginia 22060
147. T. F. Widmer, Thermo Electron Corporation, 85 First Avenue, Waltham, Massachusetts 02173
148. E. S. Wilson, Space Nuclear Systems, AEC, Germantown, Md., 20767
149-163. Division of Technical Information Extension (DTIE)
164. Laboratory and University Division, ORO